

ADA 140383

Report MDC Q1208

INVESTIGATION OF SHORT-PULSE ELECTRON-BEAM PROPAGATION

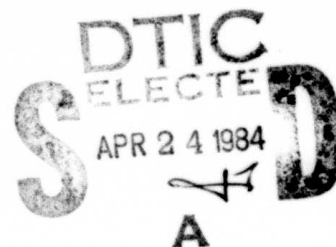
M. A. Greenspan
E. A. Rose

McDonnell Douglas Research Laboratories
St. Louis, Missouri 63166

Final Technical Report
7 December 1983
for Period 7 May 1982 - 7 December 1983

Approved for public release; distribution unlimited

Sponsored by
Defense Advanced Research Projects Agency (DoD)
ARPA Order No. 4395
Monitored by Naval Surface Weapons Center
under contract N60921-82-C-0091



DTIC FILE COPY

84 04 23 036

Disclaimer

The views and conclusions contained in this document are those of the author and should not be interpreted as representing the official policies, either expressed or implied, of the Defense Advanced Research Projects Agency of the U.S. Government.

UNCLASSIFIED

SECURITY CLASSIFICATION OF THIS PAGE (When Data Entered)

REPORT DOCUMENTATION PAGE		READ INSTRUCTIONS BEFORE COMPLETING FORM															
1. REPORT NUMBER	2. GOVT ACCESSION NO. AD A140 383	3. RECIPIENT'S CATALOG NUMBER															
4. TITLE (and Subtitle) Investigation of Short-Pulse Electron Beam Propagation		5. TYPE OF REPORT & PERIOD COVERED Final Report 7 May 1982-7 December 1983															
7. AUTHOR(s) M. A. Greenspan E. A. Rose		6. PERFORMING ORG. REPORT NUMBER MDC Q1208															
9. PERFORMING ORGANIZATION NAME AND ADDRESS McDonnell Douglas Research Laboratories McDonnell Douglas Corporation St. Louis, MO 63166		8. CONTRACT OR GRANT NUMBER(s) N60921-82-C-0091															
11. CONTROLLING OFFICE NAME AND ADDRESS Defense Advanced Research Projects Agency 1400 Wilson Boulevard, Arlington, Virginia 22209 Attn: Program Management/MIS		10. PROGRAM ELEMENT, PROJECT, TASK AREA & WORK UNIT NUMBERS 61101E; 0; 0; OR40AA															
14. MONITORING AGENCY NAME & ADDRESS (if different from Controlling Office) Naval Surface Weapons Center White Oak, Silver Spring, Maryland 20910 Attn: Code R401		12. REPORT DATE 7 December 1983															
		13. NUMBER OF PAGES 47															
		15. SECURITY CLASS. (of this report) UNCLASSIFIED															
		15a. DECLASSIFICATION/DOWNGRADING SCHEDULE															
16. DISTRIBUTION STATEMENT (of this Report) Approved for public release; distribution unlimited																	
17. DISTRIBUTION STATEMENT (of the abstract entered in Block 20, if different from Report)																	
18. SUPPLEMENTARY NOTES																	
19. KEY WORDS (Continue on reverse side if necessary and identify by block number) <table border="0"> <tr> <td>Electron beam propagation</td> <td>Electron beam ionization</td> <td>Dipole decay time</td> </tr> <tr> <td>Relativistic electron beam</td> <td>Avalanche ionization</td> <td>Plasma conductivity</td> </tr> <tr> <td>Nose erosion</td> <td>Beam current</td> <td>Monopole decay time</td> </tr> <tr> <td>Hose stability</td> <td>Plasma current</td> <td></td> </tr> <tr> <td>Ion-focused regime</td> <td>Pressure window</td> <td></td> </tr> </table>			Electron beam propagation	Electron beam ionization	Dipole decay time	Relativistic electron beam	Avalanche ionization	Plasma conductivity	Nose erosion	Beam current	Monopole decay time	Hose stability	Plasma current		Ion-focused regime	Pressure window	
Electron beam propagation	Electron beam ionization	Dipole decay time															
Relativistic electron beam	Avalanche ionization	Plasma conductivity															
Nose erosion	Beam current	Monopole decay time															
Hose stability	Plasma current																
Ion-focused regime	Pressure window																
20. ABSTRACT (Continue on reverse side if necessary and identify by block number) Experiments were performed studying the propagation of a 1-MeV, 2-8 kA, 10-ns electron beam, and possible comparisons of our data with theory are recommended. Radial boundary conditions were varied by performing experiments in a glass guide tube 7.6 cm in diameter, the same tube with a conducting screen inside, and a 3.4-m-diam vacuum chamber.																	

CONTINUED

DD FORM 1 JAN 73 1473

EDITION OF 1 NOV 65 IS OBSOLETE

UNCLASSIFIED

SECURITY CLASSIFICATION OF THIS PAGE (When Data Entered)

20. Abstract (Continued)

In the glass tube with no screen, a 6-kA beam propagates well in air in a window of pressures between 200 and 1070 Pa. Net current is ~ 1 kA, with the return current largely within the beam volume. The high-pressure limit of the window is reduced for smaller beam current.

With the conducting screen inside the tube, good propagation is still observed for pressures of 200 to 1070 Pa. In addition, ion-focused propagation is observed at lower pressure, with net current equal to beam current. A "notch" in propagated current is observed for pressure \cdot time products of ~ 100 Pa-ns. As the pressure is increased above 1070 Pa, hose instability is observed and net current approaches the beam current.

Propagation in the 3.4-m-diam chamber was rectilinear at ~ 540 Pa. Hose instability occurred at higher pressures; at lower pressures the beam was stable but the path was not straight or consistent from shot to shot.

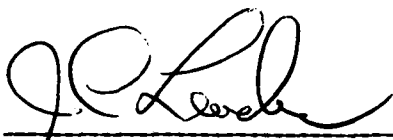
For pressures within the 200- to 1070-Pa pressure window, the front velocity increased with increasing pressure and decreasing beam current. However, for pressures greater than 2000 Pa, the front velocity decreased with increasing pressure. Net currents in the pressure window were in the beam direction over a broad radial profile of ~ 2.5 cm radius, much larger than the beam radius.

PREFACE

This final report is an account of the work completed at the McDonnell Douglas Research Laboratories on Naval Surface Weapons Center Contract No. N60921-82-C-0091, sponsored by Defense Advanced Research Projects Agency (DoD) ARPA Order No. 4395.

The work was conducted in the Radiation Sciences Department, managed by Dr. J. C. Leader. The principal investigator was Dr. M. A. Greenspan. The program monitor was Dr. C. M. Huddleston, Naval Surface Weapons Center.

This report has been reviewed and approved.



Dr. J. C. Leader
Chief Scientist, Radiation Sciences
McDonnell Douglas Research Laboratories



Dr. D. P. Ames
Staff Vice President
McDonnell Douglas Research Laboratories



Dr. C. M. Huddleston
Naval Surface Weapons Center



A1

Abstract

Experiments were performed studying the propagation of a 1-MeV, 2-8 kA, 10-ns electron beam, and possible comparisons of our data with theory are recommended. Radial boundary conditions were varied by performing experiments in a glass guide tube 7.6 cm in diameter, the same tube with a conducting screen inside, and a 3.4-m-diam vacuum chamber.

In the glass tube with no screen, a 6-kA beam propagates well in air in a window of pressures between 200 and 1070 Pa. Net current is ~ 1 kA, with the return current largely within the beam volume. The high-pressure limit of the window is reduced for smaller beam current.

With the conducting screen inside the tube, good propagation is still observed for pressures of 200 to 1070 Pa. In addition, ion-focused propagation is observed at lower pressure, with net current equal to beam current. A "notch" in propagated current is observed for pressure \cdot time products of ~ 100 Pa-ns. As the pressure is increased above 1070 Pa, hose instability is observed and net current approaches the beam current.

Propagation in the 3.4-m-diam chamber was rectilinear at ~ 540 Pa. Hose instability occurred at higher pressures; at lower pressures the beam was stable but the path was not straight or consistent from shot to shot.

For pressures within the 200- to 1070-Pa pressure window, the front velocity increased with increasing pressure and decreasing beam current. However, for pressures greater than 2000 Pa, the front velocity decreased with increasing pressure. Net currents in the pressure window were in the beam direction over a broad radial profile of ~ 2.5 cm radius, much larger than the beam radius.

TABLE OF CONTENTS

	<u>Page</u>
I. INTRODUCTION.....	1
II. EXPERIMENTAL EQUIPMENT.....	3
A. MDRL Electron-Beam Generator (MEDEA).....	3
B. Diagnostics.....	5
III. EXPERIMENTAL RESULTS.....	9
A. General Phenomenology.....	9
B. Pressure Window Measurements.....	11
C. Front Velocity Measurements.....	14
D. Low-Pressure Propagation.....	18
E. Magnetic Field Measurements.....	22
IV. SUMMARY AND CONCLUSIONS.....	32
V. RECOMMENDATIONS.....	33
REFERENCES.....	34

LIST OF ILLUSTRATIONS

<u>Figure</u>	<u>Page</u>
1. Diagram of MDRL electron-beam generator (MEDEA).....	1
2. Typical oscillograms of MEDEA diode voltage (upper trace) and injected current (lower trace).....	4
3. Arrangement for experiments in 7.6-cm-diam glass guide tube.....	5
4. Arrangement for experiments in 3.4-m-diam controlled-environment chamber.....	6
5. Faraday cup/calorimeter combination.....	7
6. (a) Magnetic-field probe, (b) typical probe response to a 250-ps-rise-time magnetic-field step, and (c) typical probe signal showing \vec{B}_0 at a pressure of 27 Pa with probe at a radial position of 3 cm.....	8
7. Open-shutter photographs of e-beam propagation in 7.6-cm-diam glass guide tube with no screen.....	9
8. Open-shutter photographs of e-beam propagation in 7.6-cm-diam glass guide tube with conducting screen inside.....	10
9. Open-shutter photographs from camera 1 of e-beam propagation in 3.4-m-diam controlled-environment chamber.....	12
10. Pressure windows for MEDEA e-beam propagation at 6 kA current in four different gases.....	13
11. Comparison of pressure windows in neon of FX-25 and MEDEA e-beams. The data points with circles and squares represent MEDEA data taken on different days, with the circles representing data taken with a worn cathode and the squares, data taken after the cathode was polished.....	13
12. Pressure windows for MEDEA e-beam in air in 7.6-cm-diam glass guide tube with conducting screen liner. Data are shown for two values of beam current: (a) $I_b = 8$ kA, and (b) $I_b = 3$ kA.....	15
13. Typical Faraday cup data used to determine beam front velocity. A graph of front arrival time (t_f) is inset in the larger graph.....	16
14. Faraday cup data showing the variation of front arrival time with pressure from $P = 270$ to $P = 2400$ Pa. The front velocity increases with increasing pressure in this regime.....	17
15. Faraday cup data at high pressures showing the front velocity decreasing with increasing pressure.....	19
16. Measured front velocity as a function of pressure at two values of beam current.....	19

<u>Figure</u>	<u>Page</u>
17. Faraday cup data at low pressure showing ion-focused-regime propagation, charge-neutral propagation, and a "notch" in propagated current, possibly due to the two-stream instability.....	20
18. Net current as a function of time at air pressures of (a) 400 Pa and (b) 1070 Pa. Beam current is shown for comparison. The data were measured at an axial position of 212 cm, with no screen in the guide tube.....	23
19. Radial dependence of net current at air pressures of (a) 400 Pa and (b) 1070 Pa.....	25
20. Net current as a function of time at various air pressures from 29 to 1070 Pa. Beam current is shown for comparison. The guide tube was lined with a conducting screen.....	27
21. Net current as a function of time, weighted by a geometrical factor because of hose oscillations by the beam. Beam current is shown for comparison.....	28
22. Net current data with screen inside glass drift tube at a higher beam current ($I_{\text{beam}} \cong 8 \text{ kA}$).....	31

LIST OF TABLES

<u>Table</u>	<u>Page</u>
1. Front velocity vs pressure compared for two values of beam current. Data were taken in the guide tube with no screen.....	17
2. Front velocity vs pressure compared for two values of beam voltage. Data were taken in the guide tube with no screen.....	18

I. INTRODUCTION

The primary purpose of this investigation was to increase the data base on electron-beam propagation phenomena in an easily obtained parameter regime (beam voltage of ~ 1 MV, current of 2-8 kA, and duration of ~ 10 ns FWHM). Particular attention was given to phenomena considered relevant to the Chair Heritage program, such as nose erosion, hose stability at high pressure, ion-focused-regime propagation, net current measurement, and plasma conductivity generation.

A number of distinctive features characterize this work in an admittedly often-explored parameter regime. First, our electron-beam generator has a voltage rise time at injection of ~ 2 ns, permitting us to study nose erosion phenomena with a beam which quickly reaches a steady state at the nose. This feature permitted beam front velocity measurements with an accuracy of $\sim 3\%$ over a broad range of conditions, including variations of gas pressure, beam current, and voltage. Second, three different radial boundary conditions were studied: a 7.6-cm-diam glass guide tube, the same tube with a copper screen inside, and a 3.6-m-diam controlled-environment (vacuum) chamber. Third, in the case of the guide tube with the conducting screen, propagation was adequate up to 13 kPa (100 Torr) of air to measure front velocity and net current. Particularly at lower currents (~ 3 kA), propagation was observed at sufficiently high pressure that (a) there was little avalanche ionization, (b) the net current was nearly equal to beam current, (c) the front velocity decreased with increasing pressure, and (d) growing hose oscillations were detected with the magnetic probes.

Although this investigation did not include significant theoretical work, we believe that existing propagation simulation programs could be used to compare predicted results with significant portions of the data to test the physics assumptions.

In related IRAD (independent research and development) investigations, the beam current density radial profile has been measured under certain conditions using x rays emitted when the beam strikes a tungsten wire target (dubbed a "bow probe" at Lawrence Livermore National Laboratory, Reference 1). Also, a hot, reduced-density channel formed by the beam has been suc-

cessfully observed using laser deflection measurements. Where helpful, results of these investigations are cited. Details can be found in Reference 2.

This work extends that done previously for DARPA with a lower energy beam (400 keV) (Contract No. N60921-81-C-0512, Reference 3) and incorporates much of the further work suggested in the final report for that contract, particularly the measurements at higher gas pressures, and radially resolved beam and net current profiles. The present work is authorized by Contract No. N60921-82-C-0091, P0003, ARPA Order No. 3618, Amendment No. 35.

The beam generator and diagnostic instrumentation employed in these experiments are described in Section II. Section III presents experimental results and analysis. Results are summarized in Section IV and recommendations are given in Section V.

II. EXPERIMENTAL EQUIPMENT

A. MDRL Electron Beam Generator

The MDRL electron-beam generator (MEDEA) developed under IRAD is shown in Figure 1. It operates as follows. Two 0.4 μf capacitors are charged to $\sim \pm 25$ kV and switched by a triggered spark gap into the single-turn primary of a dual-resonant transformer. The high-voltage end of the secondary winding couples to the pulse-line capacitance through the external inductor, designed to optimize the pulse line voltage. Typically, ~ 900 kV is achieved at the transformer and 1.4 MV on the pulse line. The isolation resistor minimizes pre-pulse at the diode. The output switch pressure is adjusted for self-breakdown at the peak of the pulse-line voltage, sending the voltage pulse through the isolator section to the vacuum diode. The taper on the isolator helps provide impedance matching and some voltage step-up.

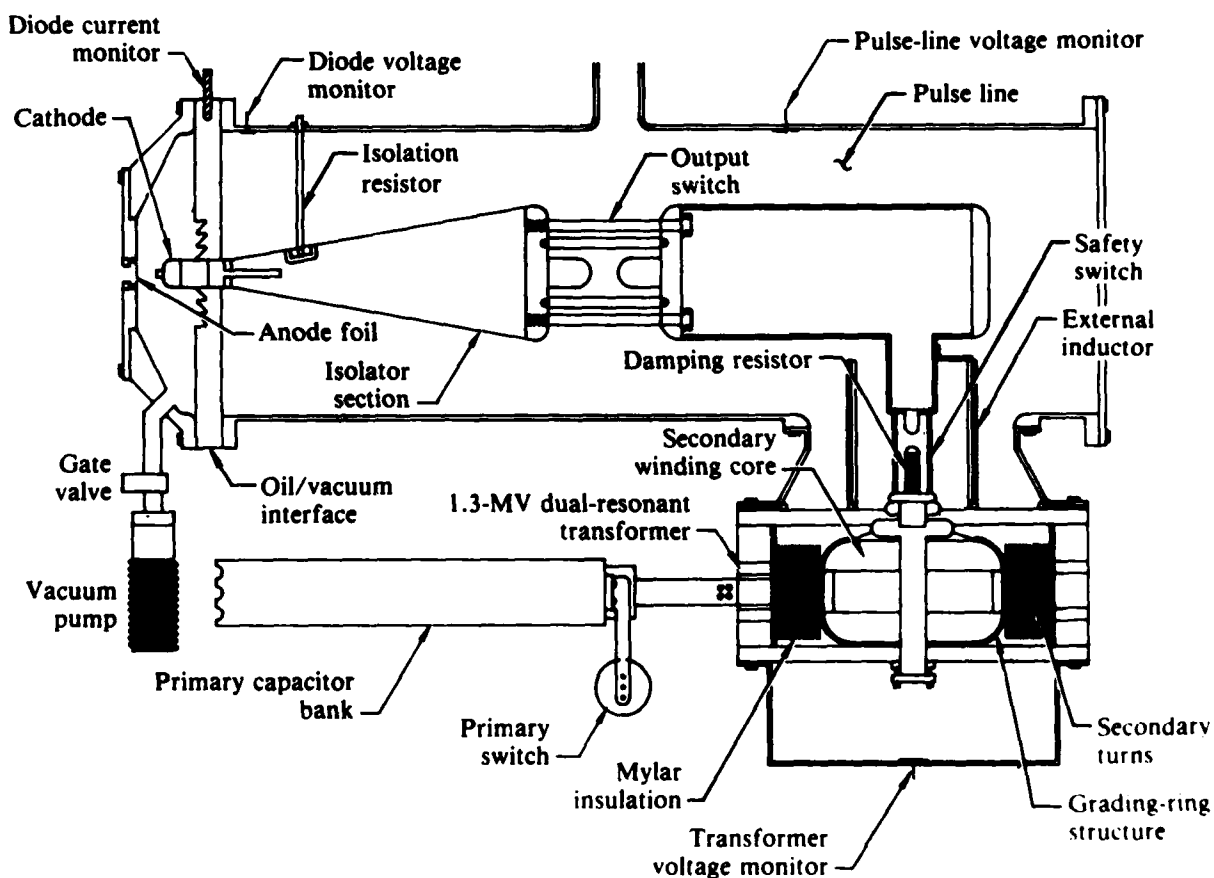


Figure 1. Diagram of MDRL electron-beam generator (MEDEA).

Typical diode voltage and injected beam currents are shown in Figure 2. The safety switch and damping resistor (placed in parallel with the external inductor) prevent ringing of the energy stored in the internal capacitance of the transformer secondary winding. When the pulse line voltage drops to zero, the safety switch self-fires and the transformer winding discharges through the damping resistor, output switch, and either the diode or isolation resistor.

Pulse-to-pulse reproducibility is usually within $\sim \pm 2\%$ for diode voltage and output current.

Bow-probe data taken with 400 Pa of air in the insulating guide tube show that the beam is $\lesssim 1$ cm in diameter after 30 cm of propagation, and after 255 cm of propagation it is very close to a Bennett profile, i.e., $J_b \propto (1 + r^2/a^2)^{-2}$, where J_b is the beam current density and a , the Bennett radius, is 0.5 cm. At 1070 Pa the beam appeared more tightly pinched, but the bow-probe data inversion is incomplete as of this writing.

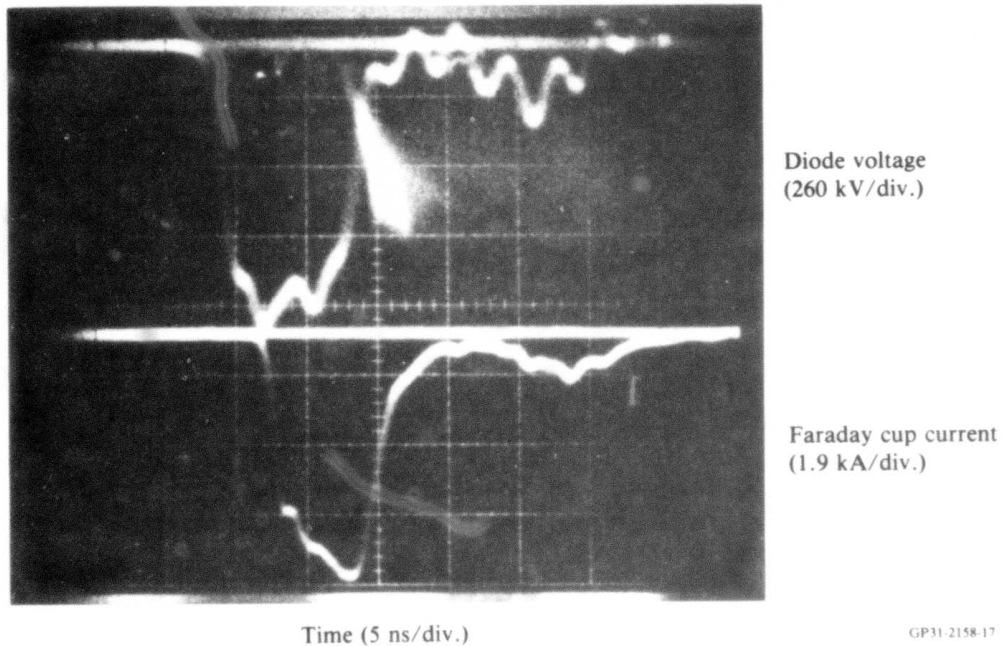


Figure 2. Typical oscillograms of MEDEA diode voltage (upper trace) and injected current (lower trace).

The arrangement for experiments in the guide tube is shown in Figure 3 and for experiments in the large chamber in Figure 4.

B. Diagnostics

The diagnostics used for this experiment consisted of a Faraday cup/calorimeter, magnetic-field probes, open-shutter photography, and diode voltage and current monitors. Two other diagnostics (bremsstrahlung emission from a tungsten wire crossing the beam, and laser-deflection measurements of the reduced-density channel) were also developed under MDRL IRAD and preliminary IRAD results are quoted here as needed.

Figure 5 shows the MDRL Faraday cup/calorimeter. It is similar to that used in our previous work with the Febetron 706 (Reference 3); the major changes are a thicker collector to stop the higher energy electrons and a reduced inductance of the lead between the collector and the output connector using a 0.6-cm-diam bellows instead of a thin wire. Calibration to $\sim \pm 3\%$ was obtained using a mercury-wetted reed switch (Tektronix 109) pulser to obtain an input signal. The Faraday cup output was compared on a sampling oscillo-

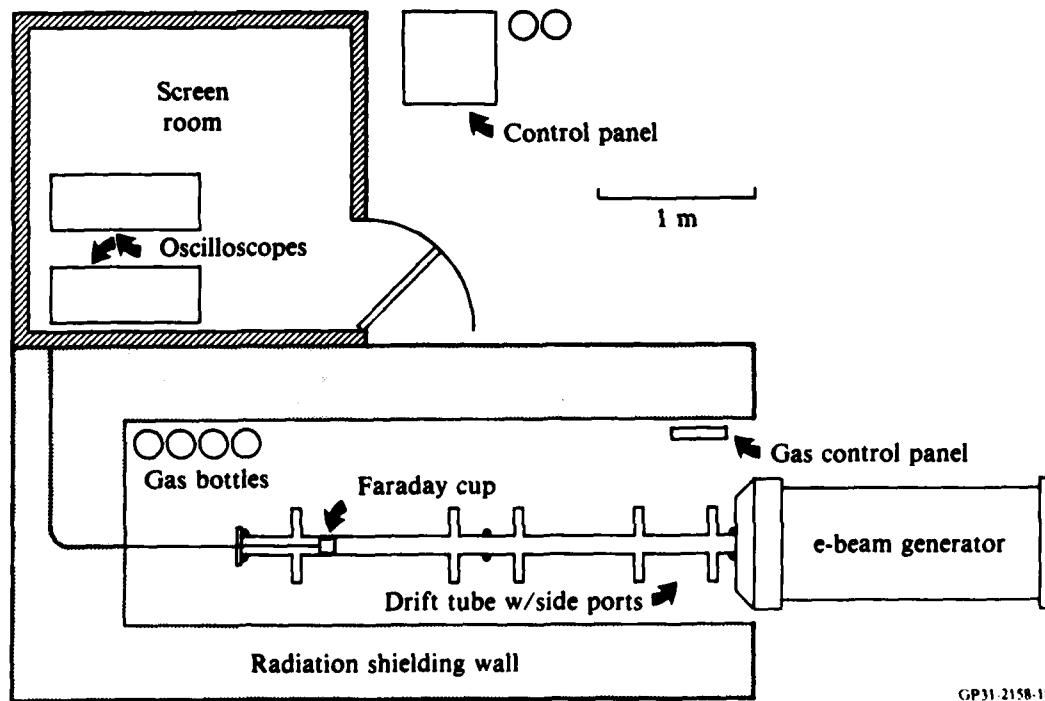


Figure 3. Arrangement for experiments in 7.6-cm-diam glass guide tube.

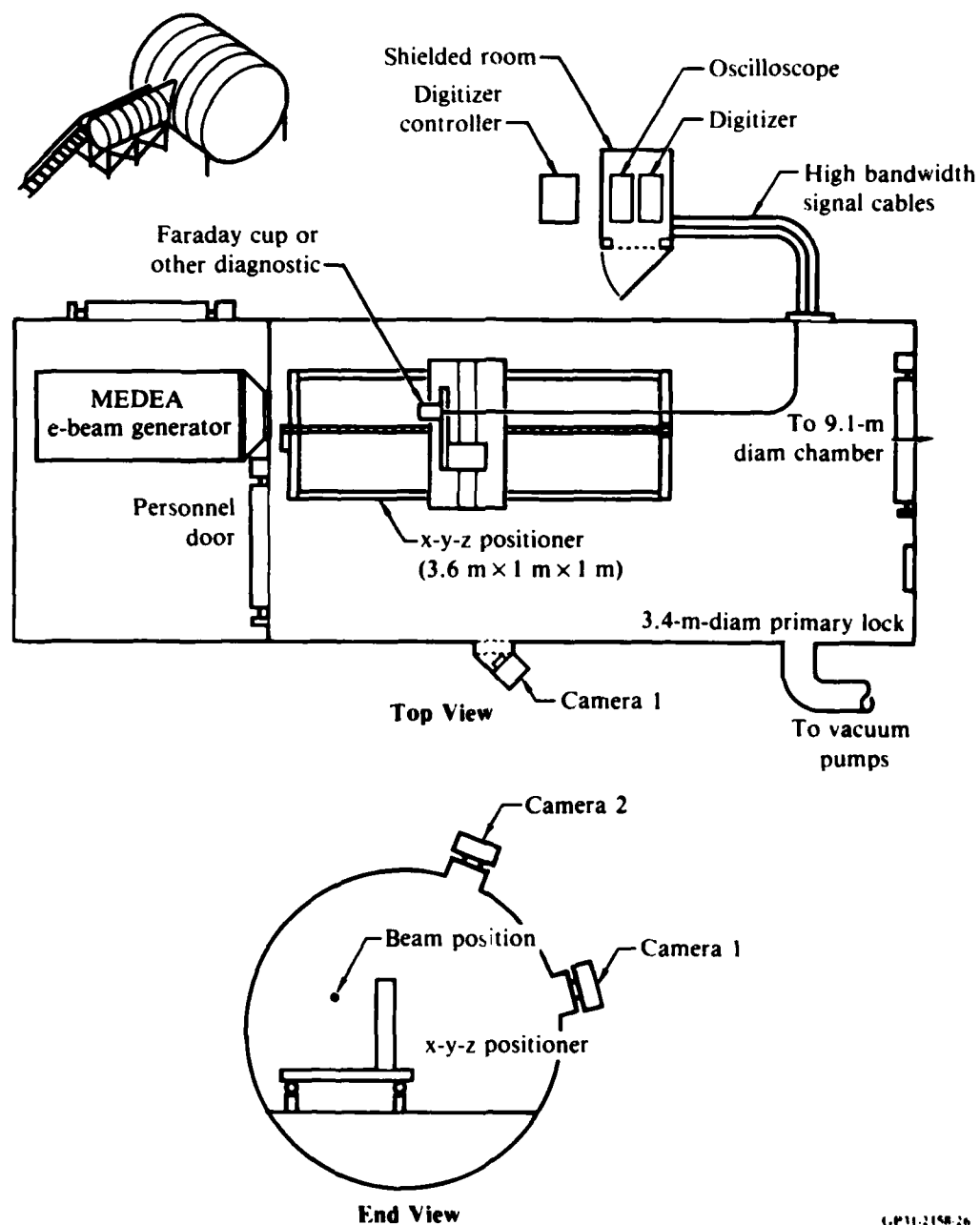
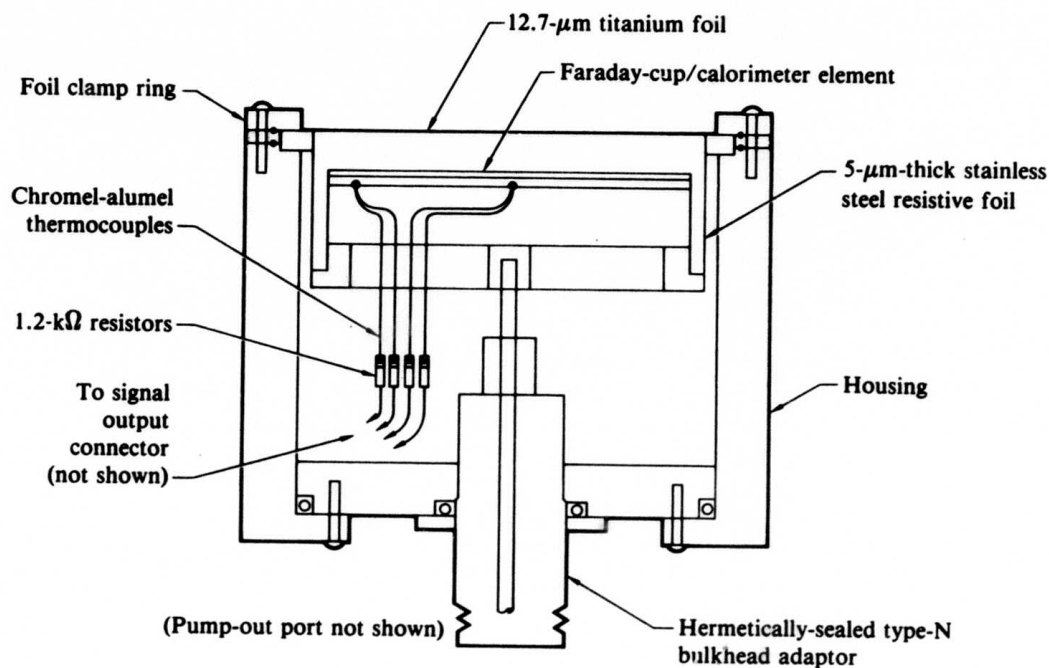


Figure 4. Arrangement for experiments in 3.4-m-diam controlled-environment chamber.

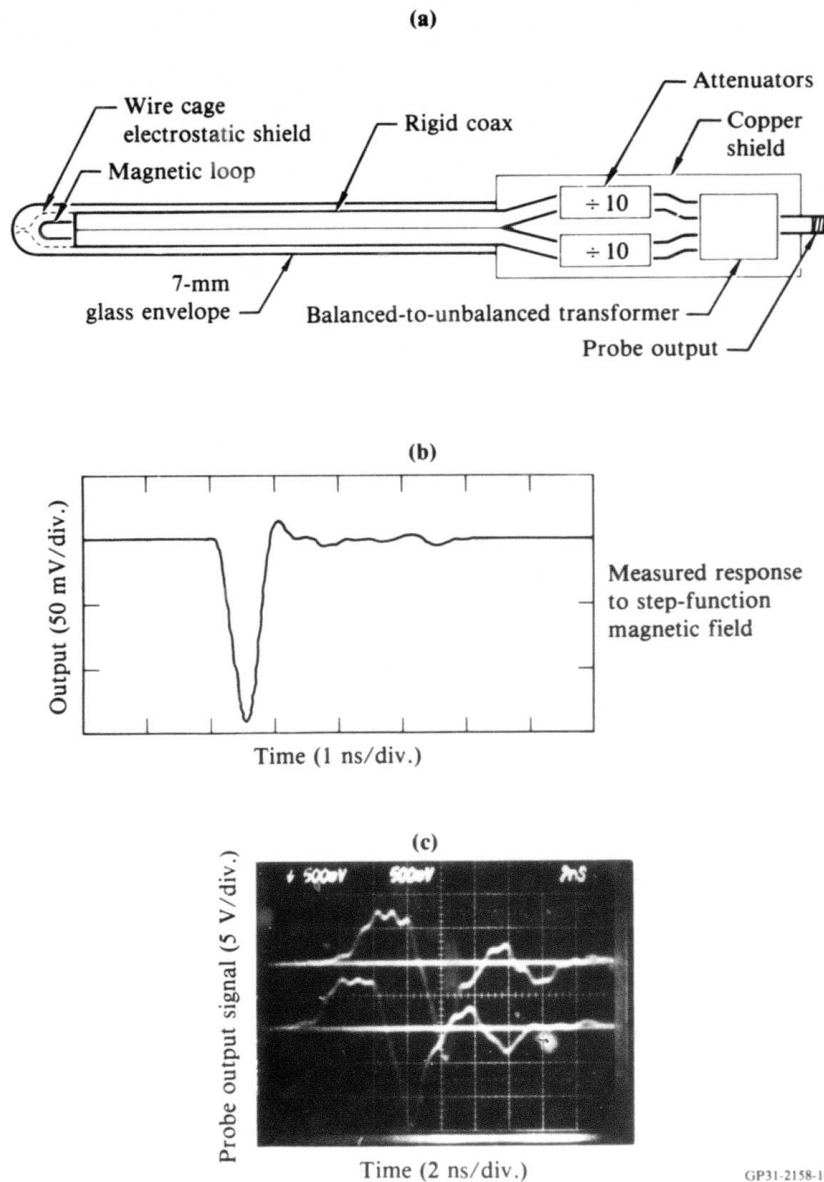


GP31-2158-21

Figure 5. Faraday cup/calorimeter combination.

scope with the output of a set of calibrated attenuators with the same input. The 10-90 rise time of the system including Faraday cup was ~ 350 ps; at this speed, the bandwidths of the pulser, the sampling scope, and the coaxial cables all combine to make further resolution difficult.

The magnetic-field probes (Figure 6a) are identical to those used previously at MDRL (Reference 3). To calibrate the probes, a step-function current was driven through a 50- Ω coaxial structure creating a step-function magnetic field in a known geometry. The probe output (Figure 6b) was then numerically integrated and compared with the input current. A typical magnetic probe signal (taken at pressure ≈ 27 Pa and probe radial position of ~ 3 cm) is shown in Figure 6c. The probe data was hand-digitized and stored on floppy discs for analysis (integration, plotting). To obtain timing information relative to Faraday cup signals, the following procedure was employed. A diode voltage monitor on the MEDEA generator produces a dV_d/dt output (V_d is the diode voltage). This signal was used to externally trigger the (Tektronix 7844) oscilloscope, and the triggering level was adjusted to minimize the timing jitter of the signals. Accuracy was comparable to that obtained by actually displaying V_d on one of the scope channels (viz., $\sim \pm .15$ ns).



GP31-2158-16

Figure 6. (a) Magnetic-field probe, (b) typical probe response to a 250-ps-rise-time magnetic-field step, and (c) typical probe signal showing B_θ at a pressure of 27 Pa with the probe at a radial position of 3 cm.

III. EXPERIMENTAL RESULTS

A. General Phenomenology

An initial understanding of the beam propagation may be gleaned from open-shutter photographs. Figures 7, 8, and 9 show a series of photographs in the three configurations, namely, the 7.6-cm-diam glass guide tube, the same tube with a conducting screen inside, and the 3.4-m-diam controlled-environment chamber. The following observations are noteworthy.

With no screen and at low pressures, the beam goes straight for a certain distance and then deflects abruptly and strikes the glass wall (Figures 7a and b); sometimes a portion bounces off the wall and strikes the wall farther on (Figure 7a). The position and direction of the "break" is consistent from shot to shot, but they depend sensitively, however, on the gas pressure. This consistency suggests that the instability causing the break grows from initial conditions at injection due to asymmetries in the diode, rather than growing

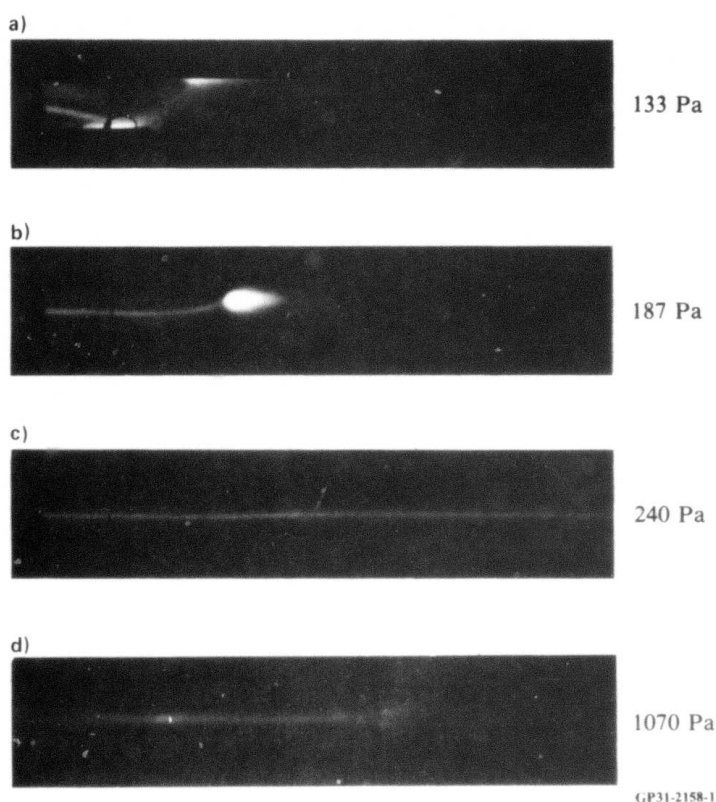


Figure 7. Open-shutter photographs of e-beam propagation in 7.6-cm-diam glass guide tube with no screen.

from thermal noise. At pressures of ~ 240 – 1070 Pa (in air), the beam propagates stably (Figure 7c). Although small bends occur the beam always re-centers itself in the drift tube in this pressure range, suggesting that the instability is stabilized by the drift-tube walls. At higher pressures (800 Pa and above, Figure 7d) part of the beam (shown below to be the tail) breaks off and strikes the wall.

With the addition of the screen inside the drift tube, a few new features appear. At low pressures ($\lesssim 30$ Pa, Figure 8a), there is stable propagation in the ion-focused regime (Reference 4). In this regime, the ion density n_i created by beam electron impact ionization is between n_b/γ^2 and n_b , where n_b is the beam electron density and γ is the usual relativistic factor. Plasma electrons are rapidly driven to the walls by the radial electric field caused

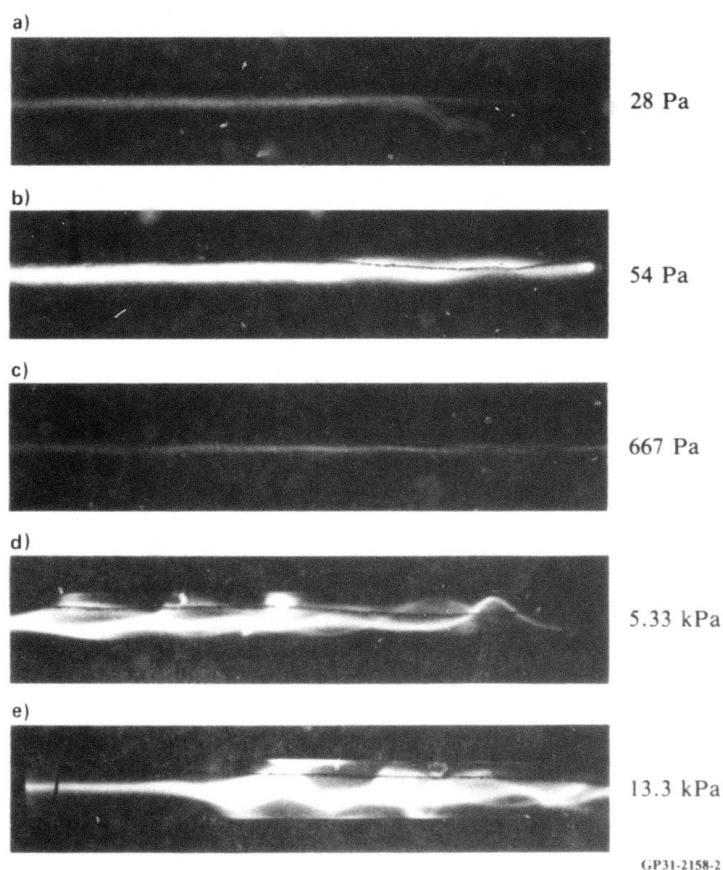


Figure 8. Open-shutter photographs of e-beam propagation in 7.6-cm-diam glass guide tube with conducting screen inside.

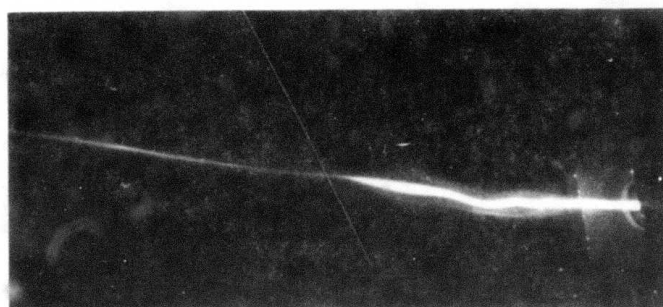
by beam space charge, leaving a reduced radial electric field inside the beam and permitting radial confinement of the beam electrons by the self-magnetic field of the beam. The screen inside the drift tube is necessary to return the charge to ground; without it, the charge produces a potential barrier sufficient to stop the beam. At higher pressures (Figures 8b) of ~ 60 Pa, color photographs show a characteristic "fire-dragon," with a reddish color and spikes pointing forward and outward from the main channel. At pressures of 270-1070 Pa, the photos are similar to those in the insulating guide tube (Figure 8c). The beam continues to propagate stably to higher pressures than without the screen, finally, however, becoming severely hose unstable (Figure 8d and 8e).

In the large chamber, the phenomena observed are similar to those observed in the insulating drift tube. The main difference is that wall stabilization does not occur. Thus, propagation at 270 Pa (Figure 9b), which in the tube appears stable, has a meandering character in the open chamber. At 540 Pa, however, propagation is straight even without the tube, within ~ 10 mrad (Figure 9c).

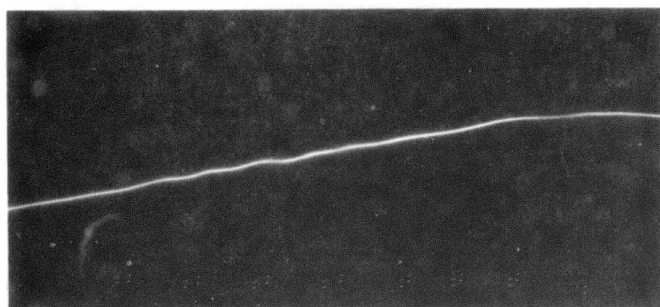
B. Pressure Window Measurements

Pressure windows for four different gases are shown in Figure 10. These were measured in the drift tube with no screen at a distance of 120 cm. The variation in position of the pressure window with gas type is qualitatively like that observed by Fessenden et al. (Reference 5) and Miller et al. (References 6 and 7). In particular, if a quantity $P_{1/2}$ is defined as a pressure below which more than half the beam charge (or energy) is lost, it is found in all three experiments that $P_{1/2}$ is proportional to the electron impact ionization cross section, σ_{ei} , for the gas ($\pm 40\%$ or so). The actual value of $P_{1/2}$ varies greatly among the experiments because of the different pulse lengths and beam currents. However, this scaling shows that the low-pressure propagation in each case depends primarily on the amount of beam-electron impact ionization produced.

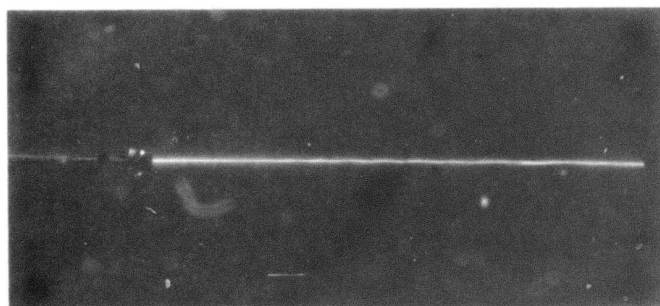
A comparison of pressure windows in neon between the experiments of Reference 5, using an FX-25 electron-beam generator, and our experiments using MEDEA is shown in Figure 11. The curves are quite similar except that the MEDEA curve is displaced by a factor of ~ 2.5 towards higher pressures. This



66 Pa



270 Pa



540 Pa



2000 Pa

G.P31-2158-25

Figure 9. Open-shutter photographs from camera 1 of e-beam propagation in 3.4-m-diam controlled-environment chamber.

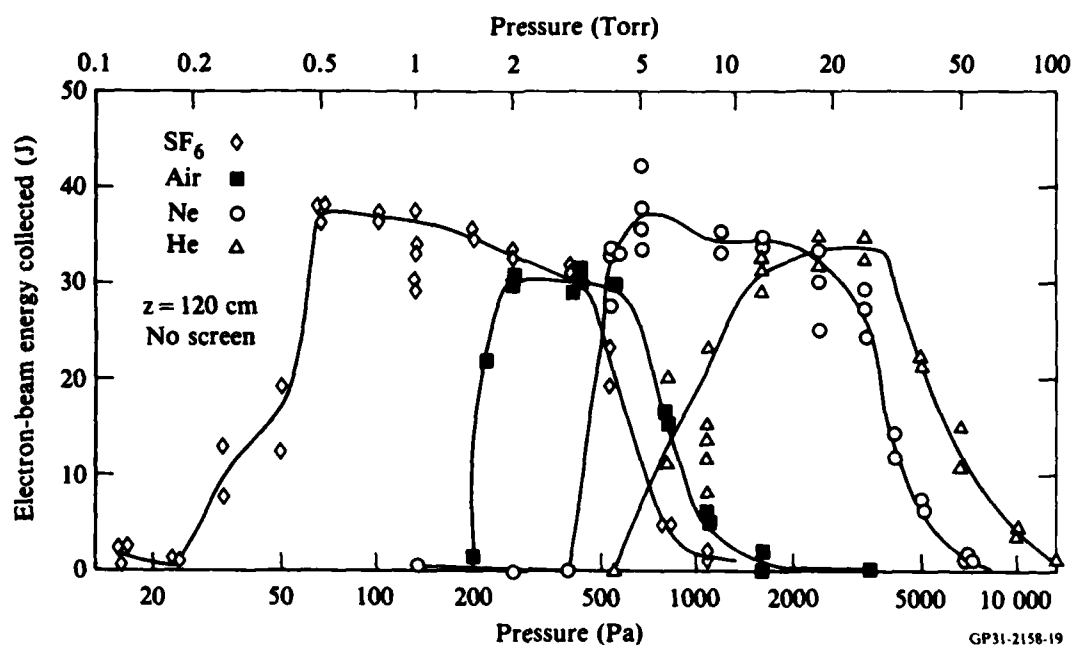


Figure 10. Pressure windows for MEDEA e-beam propagation at 6 kA current in four different gases.

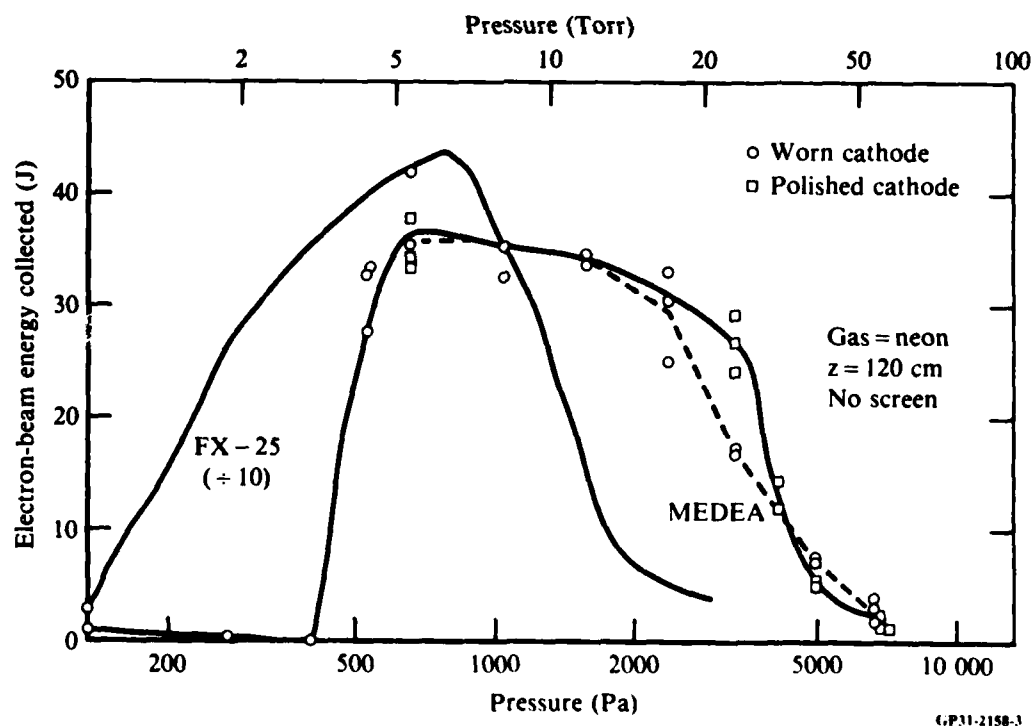


Figure 11. Comparison of pressure windows in neon of FX-25 and MEDEA e-beams. The data points with circles and squares represent MEDEA data taken on different days, with the circles representing data taken with a worn cathode and the squares, data taken after the cathode was polished.

displacement probably results primarily from the different pulse lengths of the two machines (~ 40 ns for the FX-25 compared to 10 ns for MEDEA). At low pressures the beam-generated ionization is proportional to time as well as to the electron impact ionization cross section. The longer pulse loses 10-20 ns from the front during the time that ions are being created and still has most of its energy reach the Faraday cup, whereas the shorter pulse is entirely lost. At high pressures, the shorter pulse of MEDEA is less affected by the hose instability, which grows from head to tail, and thus the pressure window extends to higher pressures.

The high end of the pressure window was found to be dependent on initial conditions. Simply polishing the cathode could increase the pressure at the high end by as much as 50%. This effect is also shown in Figure 11.

Figure 12 shows pressure windows in air for MEDEA with a screen inside the drift tube. Results are shown for two values of beam current. The window with the screen is broader than without the screen and considerably broader for the lower current. The high-pressure end of the window is caused by hose instability, as seen in the photographs and also in magnetic-probe data. At low pressures, a number of interesting phenomena occur which govern the termination of the propagation window (see Section D).

C. Front Velocity Measurements

Front velocity measurements were made in all three configurations over the range of stable propagation of the beam front. Variations with current and voltage were studied in the drift tube only. Nose erosion rates can be determined by subtracting the observed front velocities from those which would occur with no nose erosion. For a 1-MeV beam, the front velocity with no erosion would be 28.2 cm/ns.

The observed front velocity was determined from Faraday cup signals by displaying them on a dual-beam oscilloscope (Tektronix 7844) along with the diode voltage monitor signal (used to establish a fixed time reference). Timing accuracies of ± 0.15 ns were achieved with this technique. Figure 13 shows a typical data set from which a front velocity was determined. A front arrival time was defined (somewhat arbitrarily) as the time when the beam current reached 1.9 kA (0.95 kA for low-current data). The slope of the graph of front arrival time as a function of distance was then used for the front

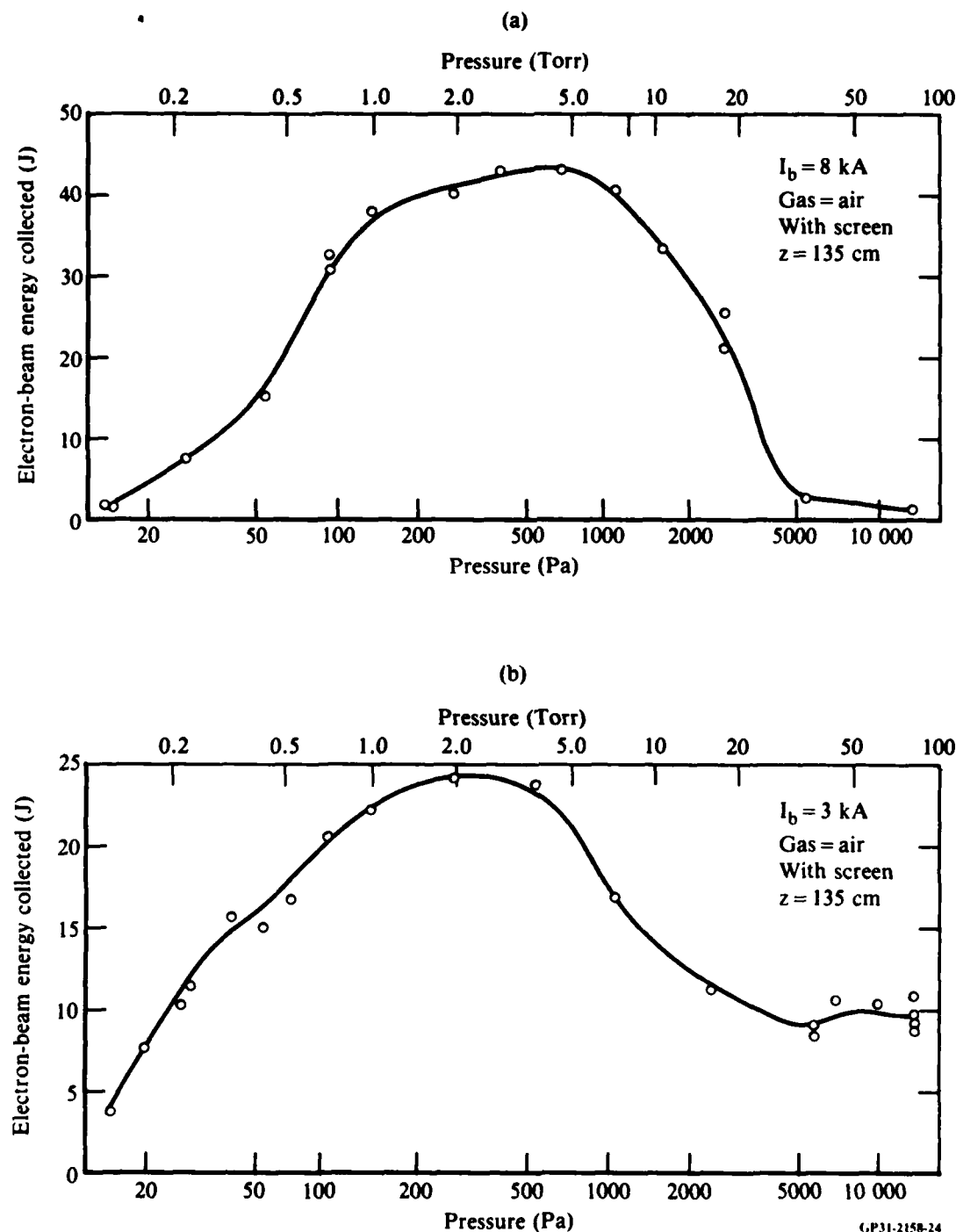


Figure 12. Pressure windows for MEDEA e-beam in air in 7.6-cm-diam glass guide tube with conducting screen liner. Data are shown for two values of beam current: (a) $I_b = 8 \text{ kA}$, and (b) $I_b = 3 \text{ kA}$.

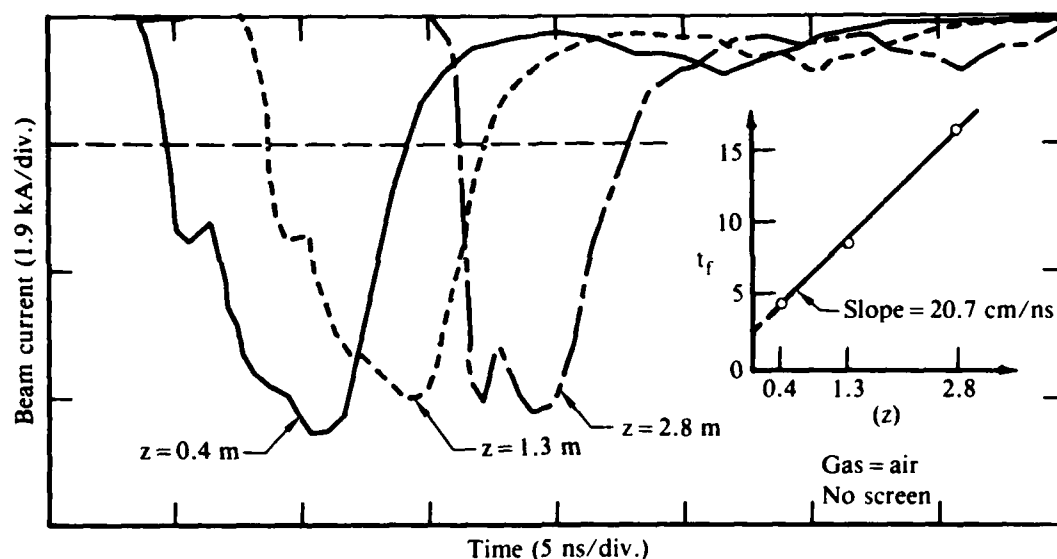
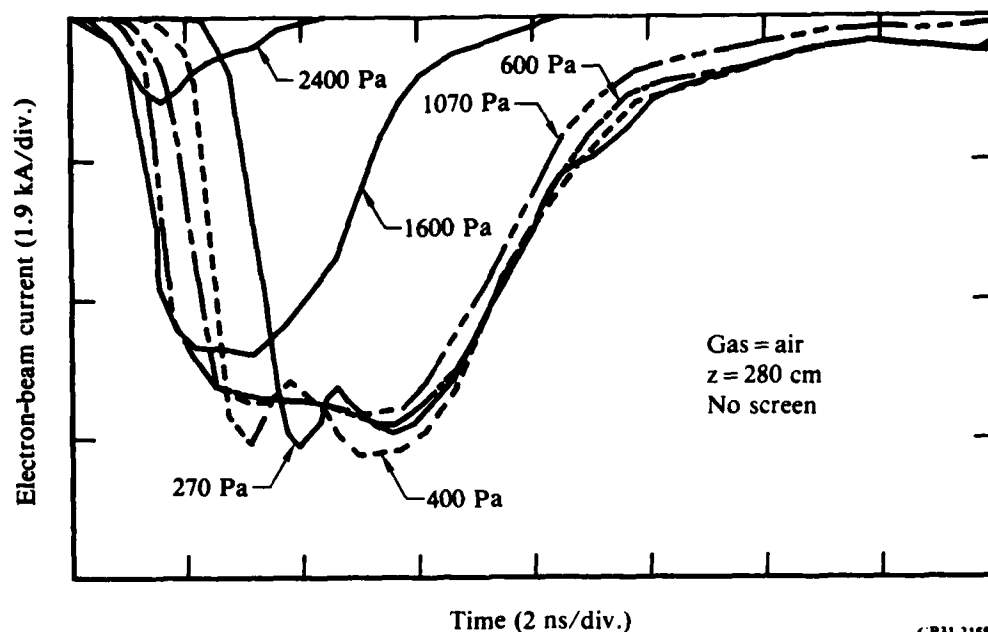


Figure 13. Typical Faraday cup data used to determine beam front velocity. A graph of front arrival time (t_f) is inset in the larger graph.

velocity. Typical variations in front arrival time with pressure can be seen from the Faraday cup data shown in Figure 14. The increase in front velocity with increasing pressure between 270 and 1600 Pa can be seen from this data.

Variations in front velocity with pressure, current, and voltage are shown in Table 1 and Table 2 for the case of the guide tube with no screen. The front velocity variation with voltage is very small, as expected ($\Delta\beta c \approx 0.2$ cm/ns for a change in voltage from 1.14 MeV to 1.27 MeV). The increase in front velocity with lower currents is expected because of the reduced energy loss from induced electric fields at the beam front. A quantitative analysis of this front velocity increase has not been performed but could be of interest.

The addition of the screen to the drift tube does not alter measured front velocities within experimental uncertainty ($\lesssim \pm .5$ cm/ns). However, front velocities could be measured over a much broader range of pressures. As the pressure was increased from 1000 to 13 000 Pa, the front velocity decreased. This decrease can probably be attributed to the effect of scattering of the beam by the gas, which can cause an increase in nose erosion



GP31-2158-5

Figure 14. Faraday cup data showing the variation of front arrival time with pressure from $P = 270$ Pa to $P = 2400$ Pa. The front velocity increases with increasing pressure in this regime.

TABLE 1. FRONT VELOCITY vs PRESSURE COMPARED FOR TWO VALUES OF BEAM CURRENT. DATA WERE TAKEN IN THE GUIDE TUBE WITH NO SCREEN.

$I_{beam} = 6 \text{ kA}, V_{beam} = 1.0 \text{ MV}$		$I_{beam} = 1.5 \text{ kA}, V_{beam} = 1.0 \text{ MV}$	
Pressure (Pa)	V_{front} (cm/ns)	Pressure (Pa)	V_{front} (cm/ns)
267	19.9	267	22.9
400	20.9	400	23.5
666	21.7	666	24.0
1066	22.2	1066	(Propagation unstable nose is lost)
1600	22.6	1600	

GP31-2158-22

TABLE 2. FRONT VELOCITY vs PRESSURE COMPARED FOR TWO VALUES OF BEAM VOLTAGE. DATA WERE TAKEN IN THE GUIDE TUBE WITH NO SCREEN.

<i>I_{beam}</i> = 2.4 kA, <i>V_{beam}</i> = 1.14 MV		<i>I_{beam}</i> = 2.4 kA, <i>V_{beam}</i> = 1.27 MV	
Pressure (Pa)	<i>V_{front}</i> (cm/ns)	Pressure (Pa)	<i>V_{front}</i> (cm/ns)
200	21.8	200	22.3
267	22.6	267	22.9
400	23.3	400	23.5
666	24.3	666	24.5
1066	24.3	1066	25.1

GP31-2158-23

(Reference 8). Faraday cup signals showing this effect are shown in Figure 15, and a plot of front velocities as a function of pressure at two values of current is shown in Figure 16.

Front velocity measurements in the space chamber were hampered by our inability to aim the beam at most pressures, as demonstrated in Figure 9. However, at 540 Pa with a beam current of 6 kA, the beam trajectory was sufficiently reproducible to permit the front velocity measurement, giving a result of 17.3 cm/ns, which is distinctly slower than in the guide tube.

D. Low-Pressure Propagation

With no conducting screen in the guide tube, the electron beam does not propagate well at air pressures below ~ 200 Pa (Figure 7), presumably because of the effects of the electrostatic potential barrier produced by the beam. With the addition of the conducting screen, there is improved propagation and a number of interesting features appear (Figure 17). Before commenting on the data, we review briefly the three propagation regimes which appear to be involved here, viz., the ion-focused regime, the two-stream unstable regime, and the stable, charge-neutral propagation regime.

Ion-focused regime (IFR) propagation (Reference 4) occurs when the beam-produced ion density (n_i) fulfills the condition

$$\frac{1}{2} < \frac{n_i}{n_b} < 1 ,$$

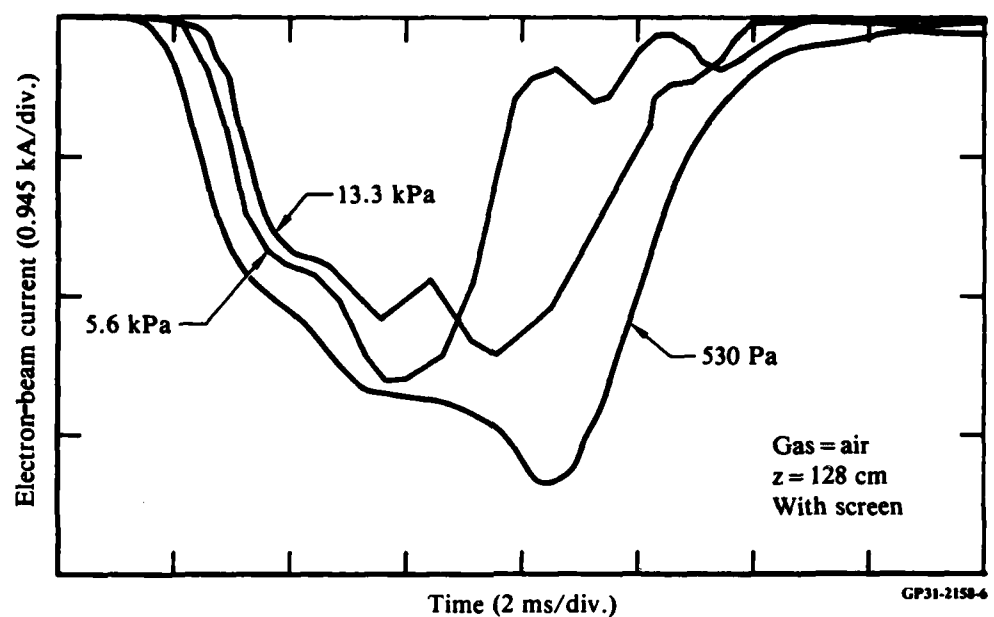


Figure 15. Faraday cup data at high pressures showing the front velocity decreasing with increasing pressure.

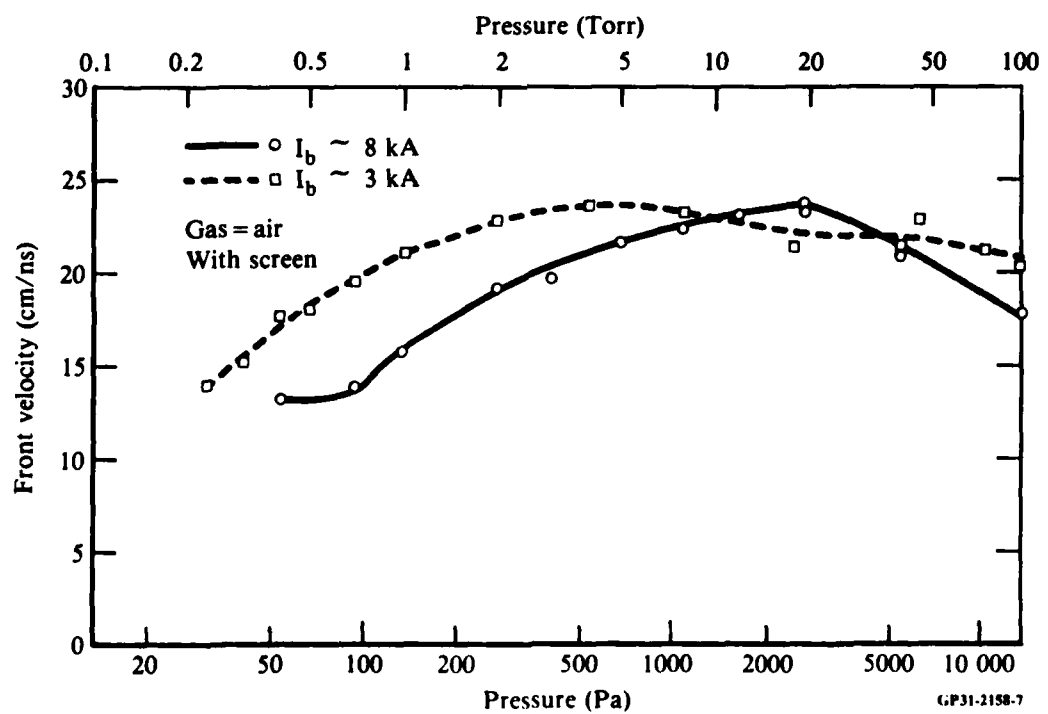


Figure 16. Measured front velocity as a function of pressure at two values of beam current.

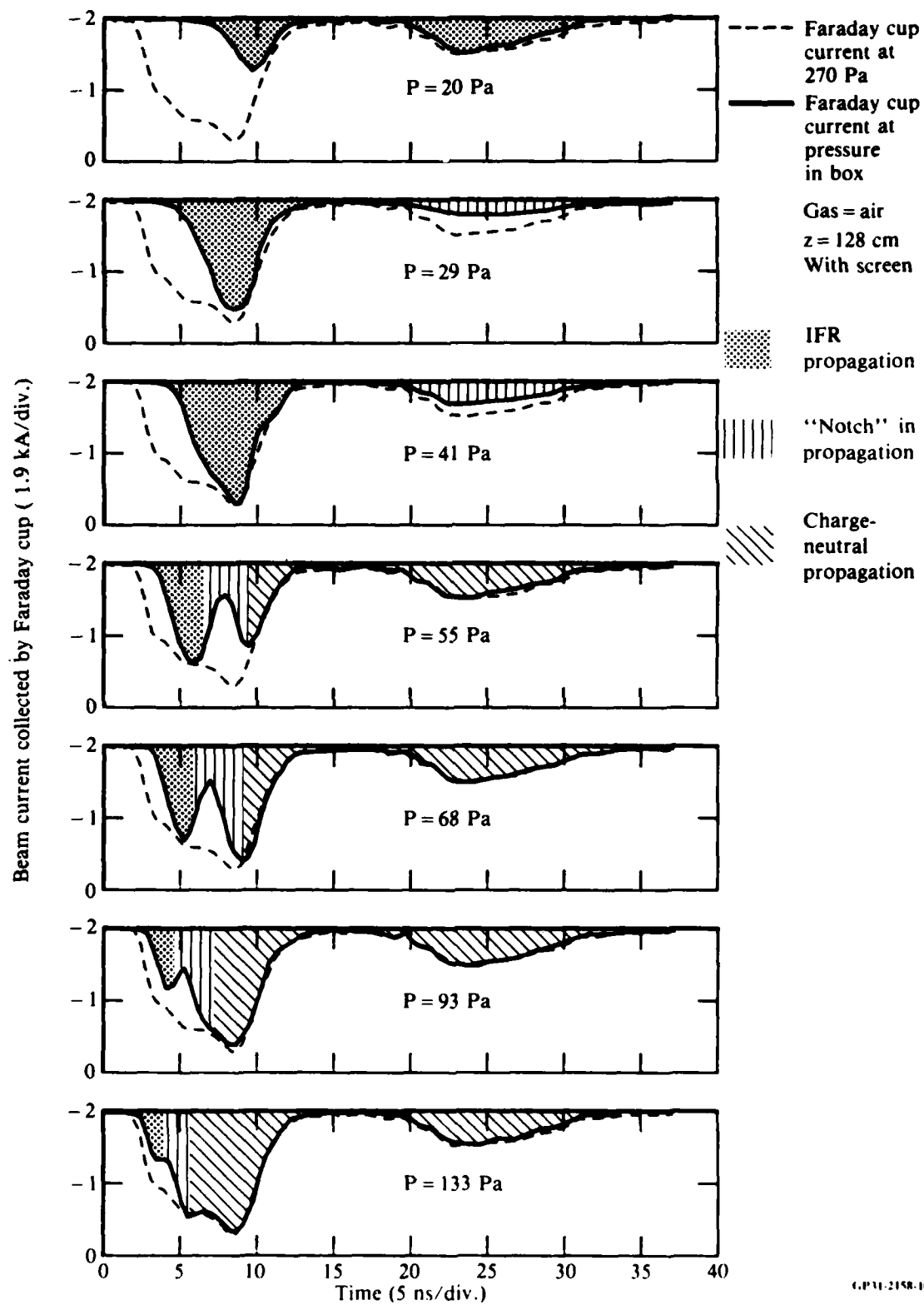


Figure 17. Faraday cup data at low pressure showing ion-focused-regime propagation, charge-neutral propagation, and a "notch" in propagated current, possibly due to the two-stream instability.

where n_b is the beam electron density and γ is the usual relativistic factor. Under these conditions, the beam is only partially charge neutralized so that a strong radial electric field exists which rapidly expels plasma electrons from the beam volume. The beam is in an equilibrium in which the outward force of the radial electric field is balanced by the $\underline{v} \times \underline{B}$ force inward.

When $n_i/n_b > 1$, the beam is completely charge neutralized and the radial electric field therefore becomes zero; plasma electrons created subsequently remain within the beam volume. The relative motion of the beam and plasma electrons can, under certain conditions, permit the growth of the two-stream instability (References 9-10) which can disrupt the propagation of the beam.

As the plasma electron density increases, the two-stream instability growth rate and saturation energy are reduced until the instability is stabilized by electron-neutral collisions. In this case the beam is in the stable, charge-neutral propagation regime.

If we consider a given axial position along the length of the guide tube, we see that the ion density increases with time, so that the beam passing through that location initially propagates in the ion-focused mode, then passes through the two-stream unstable mode, and finally reaches the stable, charge-neutral mode. As the neutral gas pressure in the tube is increased, the beam passes through the first two modes with increasing rapidity because the rate of ion production by beam-electron impact ionization is proportional to the neutral gas density.

If we consider a given slice of the beam, it will in general propagate for some distance in each regime; as the front of the beam erodes, a given slice of the beam moves closer to the beam front and thus encounters less beam-produced ionization.

To quantify these ideas, we express the ionization rate as

$$\frac{dn_i}{dt} = n_o n_b \sigma_{ei} \beta c, \quad (1)$$

where n_o is the neutral density, σ_{ei} is the electron impact ionization cross section, and βc is the speed of a beam electron. Note that avalanche ionization is neglected. In specifying the value for σ_{ei} , we assume that cascade normally associated with high electron energy impact ionization

(Reference 11) does not occur within the beam radius. Using published values of σ_{ei} and converting n_0 to units of gas pressure gives

$$\frac{dn_i}{dt} = \frac{n_b}{\tau_n}, \quad (2)$$

where $\tau_n \cong 1.3 \times 10^{-7}/P$, with P equal to air pressure in Pascals. If n_b is constant, τ_n is the time required to achieve $n_i/n_b = 1$, i.e., full charge neutralization. For a linearly rising n_b , Equation (2) shows that full neutralization is achieved after a time of $2\tau_n$.

At pressures up to 41 Pa, front velocities are slow (Figure 17a-c), attributed to the fact that neutralization times are quite long (several nanoseconds) compared to the pulse duration. The beam which reaches the Faraday cup is propagating in the ion-focused mode over most of the distance.

As the pressure is increased, the front velocity increases as the neutralization time decreases. At a point where pressure multiplied by time equals about 100 Pa-ns at the Faraday cup, there is a deep "notch" in the beam current in the data for pressures of 55 to 93 Pa, with the notch occurring sooner at the higher pressures (Figure 17d-f). This pressure multiplied by time product, 100 Pa-ns, corresponds roughly to the occurrence of full charge neutralization, necessary for onset of the two-stream instability. Finally, a short time later, efficient beam propagation occurs again, presumably because the plasma density has increased sufficiently to stabilize the two-stream instability.

Calculations and experiments which could further clarify this data are recommended in Section V.

E. Magnetic Field Measurements

Magnetic-field probe data were taken with no screen in the guide tube at pressures of 400 and 1070 Pa, and with a screen in the guide tube over a wide range of pressures (29 to 13 000 Pa) and at two values of beam current.

Net current as a function of time with no screen is shown in Figure 18. It rises for ~ 2 ns to a value of $\sim 20\%$ of the peak beam current, and then remains relatively constant for a period of time much longer than the beam duration. Radial profiles of the net current within a given radius [$(I_n(r) = 2\pi r B_\theta / \mu_0$, where B_θ is the magnetic field in the θ direction)] are

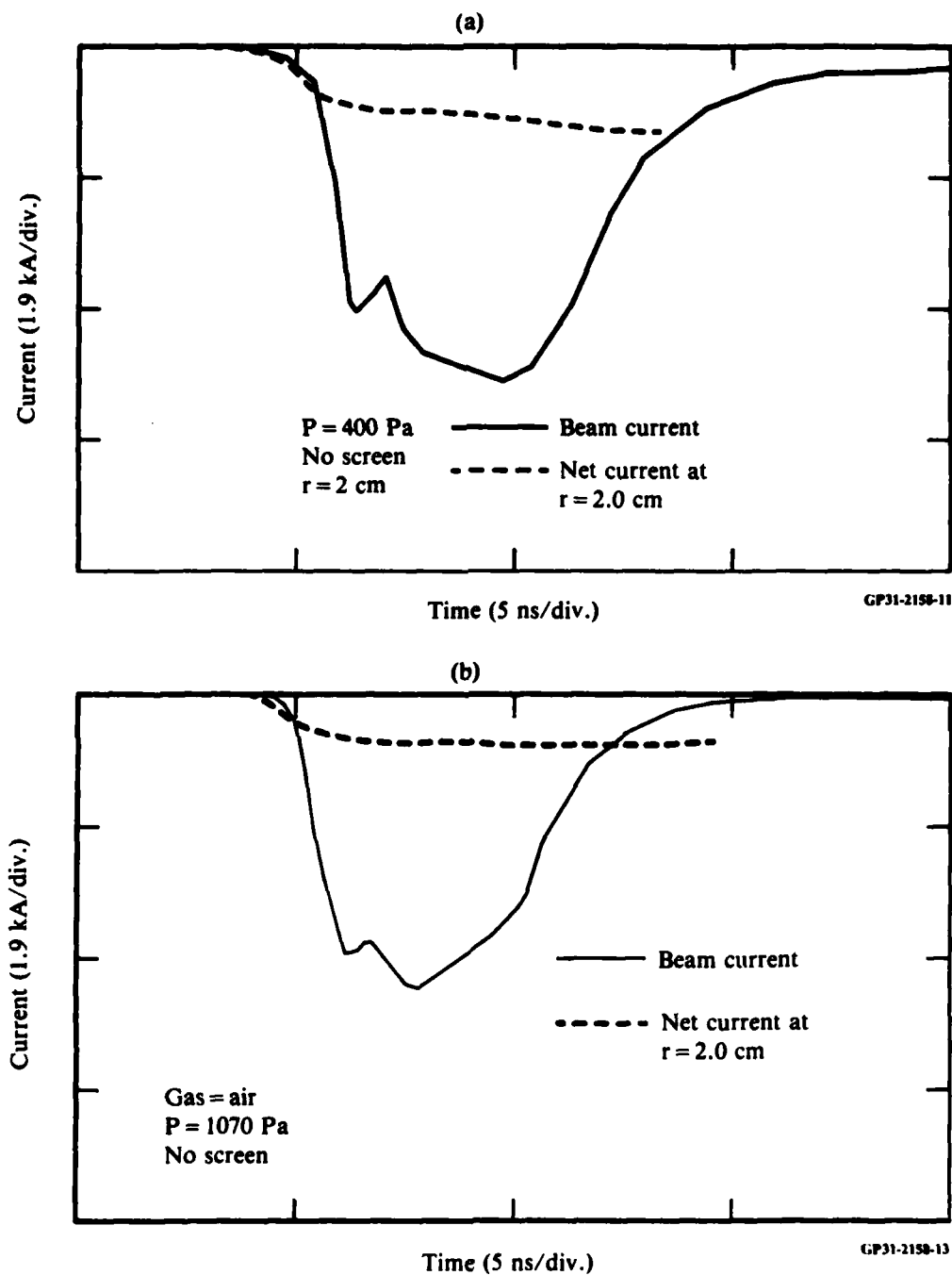


Figure 18. Net current as a function of time at air pressures of (a) 400 Pa and (b) 1070 Pa. Beam current is shown for comparison. The data were measured at an axial position of 212 cm, with no screen in the guide tube.

shown in Figure 19. The net current density, $J(r) = (1/2\pi r)(dI_n(r)/dr)$, is seen to be in the same direction as the beam out to a radius of $r \approx 2.5$ cm. This result is surprising in view of the small beam radius measured by the x-ray emission diagnostic ($\lesssim 0.5$ cm Bennett radius).

The fact that the net current is much smaller than the beam current implies that a plasma return current must be flowing opposite to the beam current direction, nearly equal in magnitude, and within a channel of $\lesssim 1$ cm in radius. On the other hand, at radii $\gtrsim 1$ cm, where the beam current density is low, the increasing net current implies that a plasma current equal to $\sim 20\%$ of the beam current is flowing in the beam direction. In contrast, a standard Ohm's law model of the plasma predicts that the plasma current should flow opposite to the beam direction in a channel somewhat larger in radius than the beam, with the details depending on the plasma conductivity profile. Two possible explanations are (1) the probes produce a large perturbation to the plasma current, or (2) the broad channel of current in the beam direction is due to δ -rays, that is, to high-energy secondary electrons produced in small-impact-parameter collisions with electrons in the neutral gas (Reference 12). This phenomenon of a broad net current flow was also observed in experiments at Lawrence Livermore National Laboratory on the ETA accelerator (Reference 12).

With the screen inside the drift tube, data were measured over the full range of pressures (from low-pressure IFR propagation to high-pressure hose-unstable propagation). Unfortunately, the "two-stream notch" regime was not explored in this survey. The radial profiles were similar to those without the screen with current flowing in the beam direction through most of the tube diameter. Data presented henceforth is at 3-cm radius, i.e., just inside the screen.

The broader pressure window and more interesting probe data were obtained at a beam current of 3 kA. Examples are shown in Figures 20 and 21. In the ion-focused regime (Figure 20a), good agreement is generally observed between probe and Faraday cup data. The small afterpulse may be caused by a two-stream-driven current late in the pulse which did not penetrate the Faraday cup foil. At 130 and 400 Pa net current is similar to, but larger than, that measured for propagation without a screen. The net current follows the beam current for a few ns and then is clamped as the plasma conductivity, σ , causes

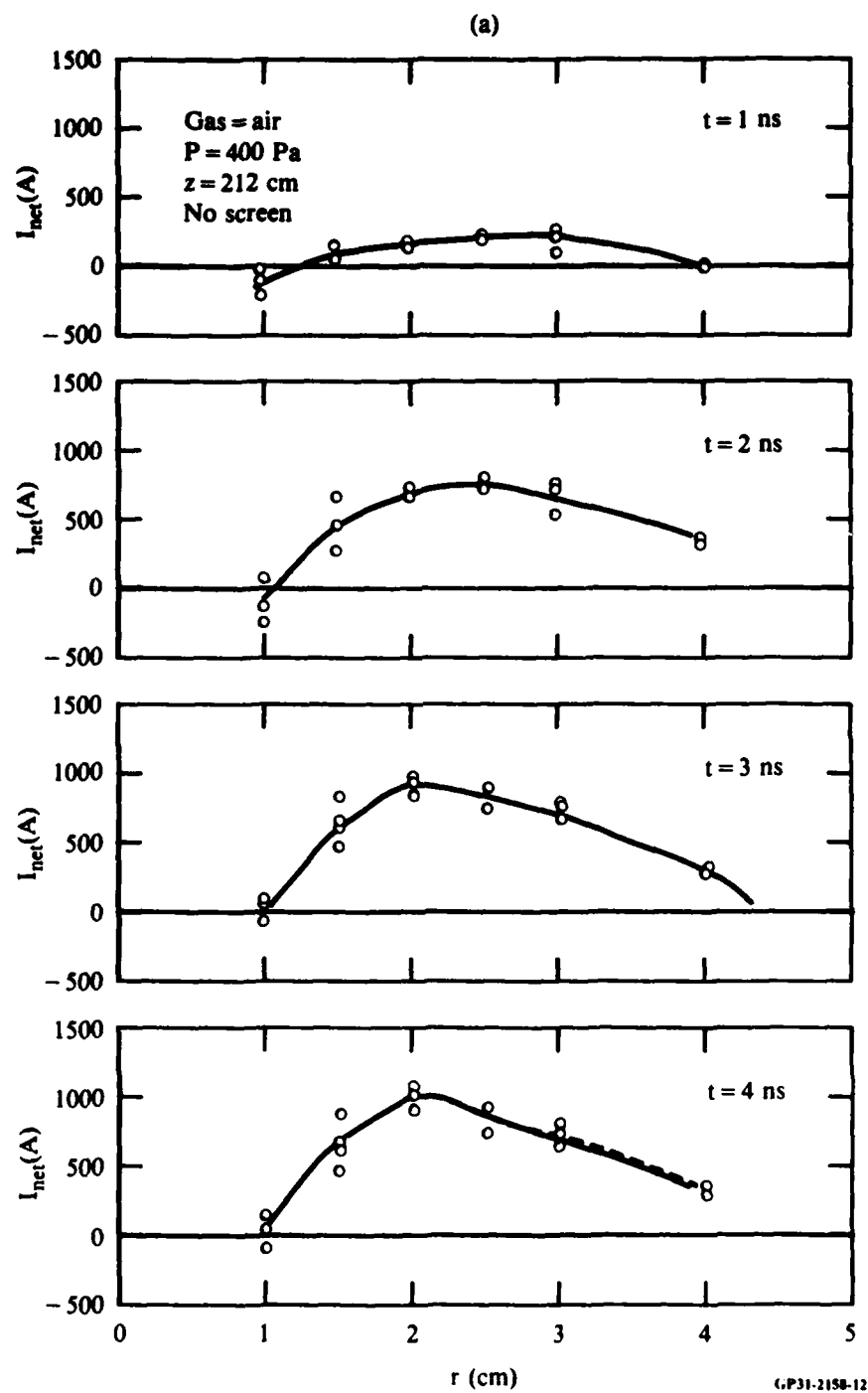


Figure 19. Radial dependence of net current at air pressures of (a) 400 Pa and (b) 1070 Pa.

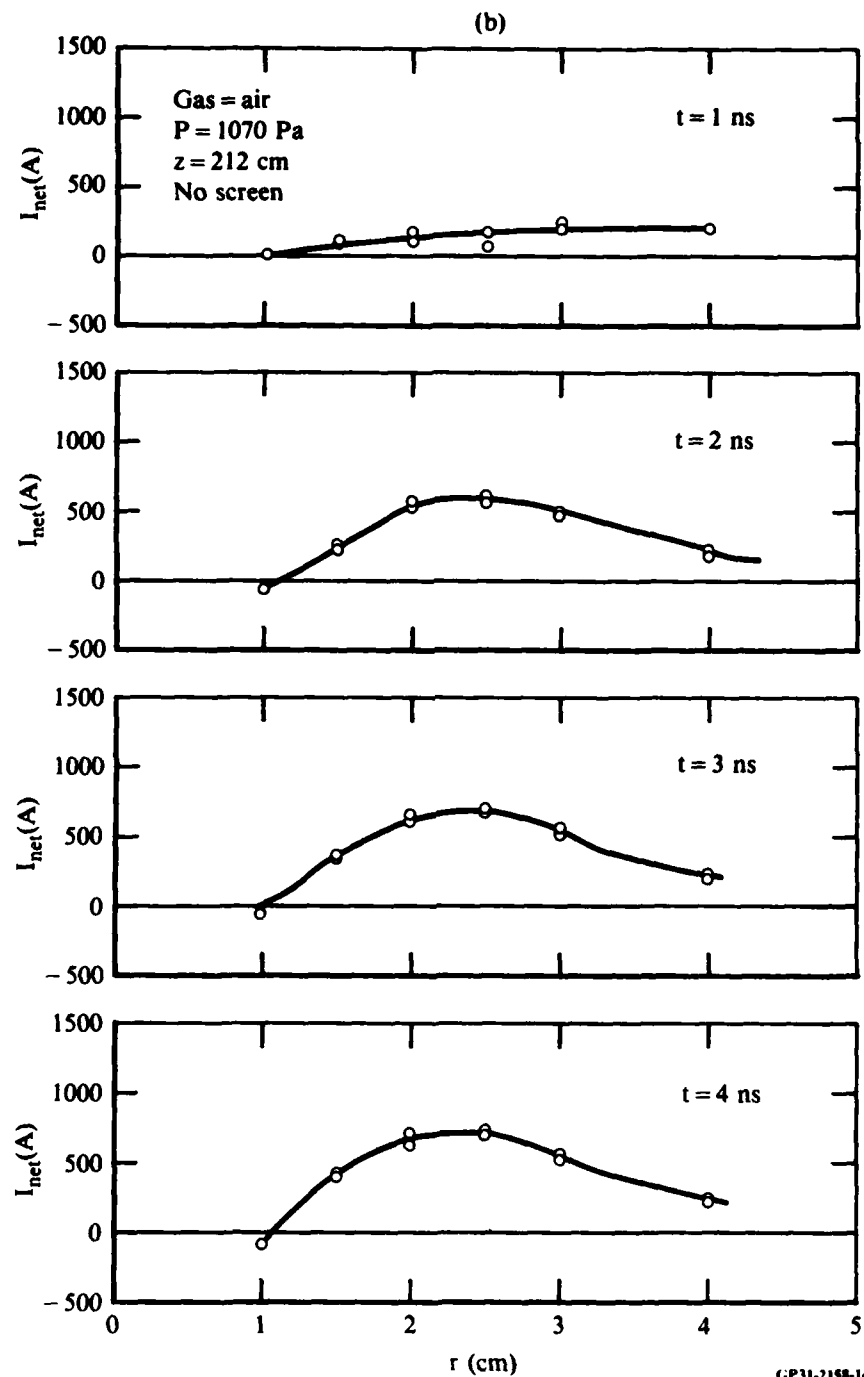
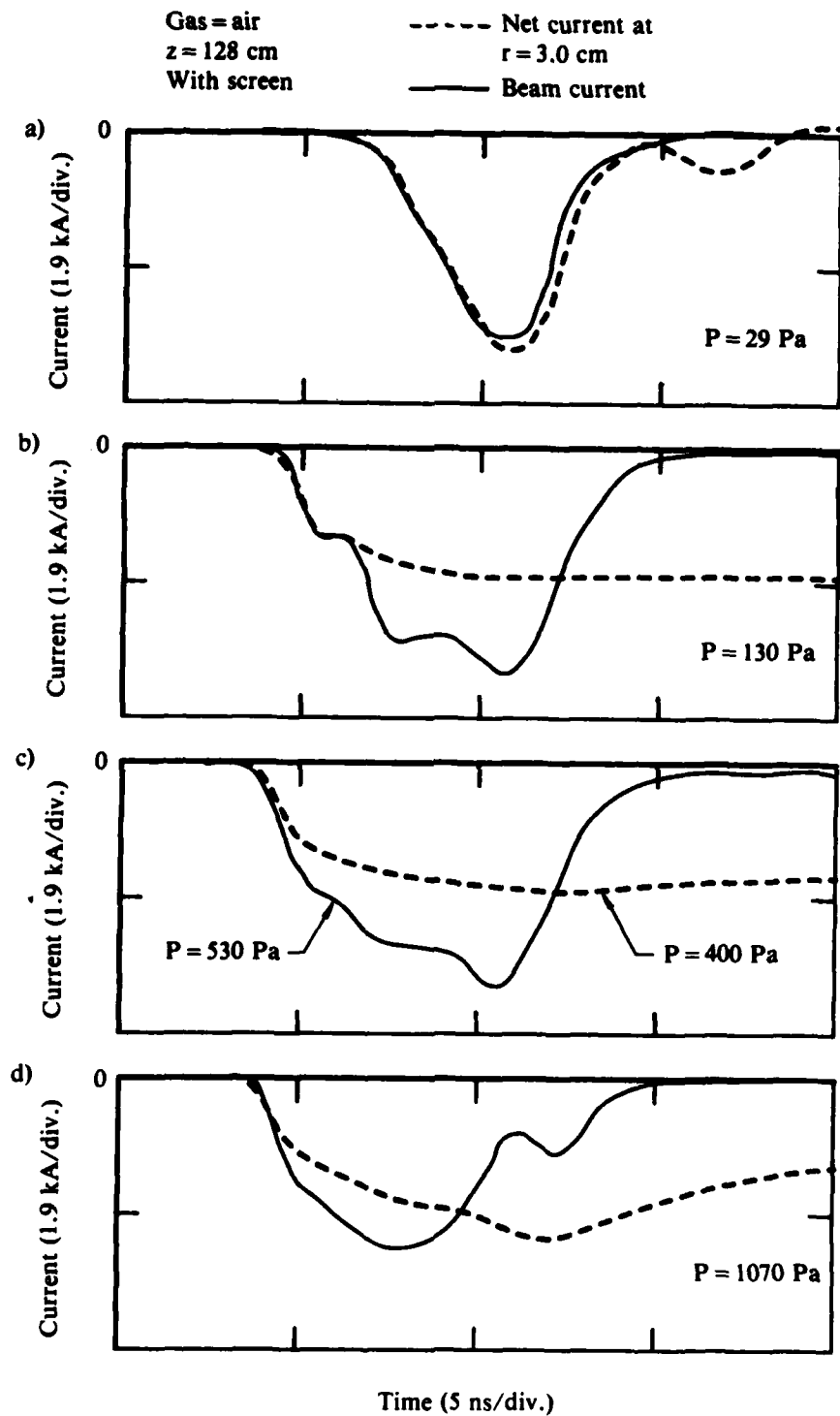


Figure 19. (Continued) Radial dependence of net current at air pressures of (a) 400 Pa and (b) 1070 Pa.



GP31-2150-8

Figure 20. Net current as a function of time at various air pressures from 29 to 1070 Pa. Beam current is shown for comparison. The guide tube was lined with a conducting screen.

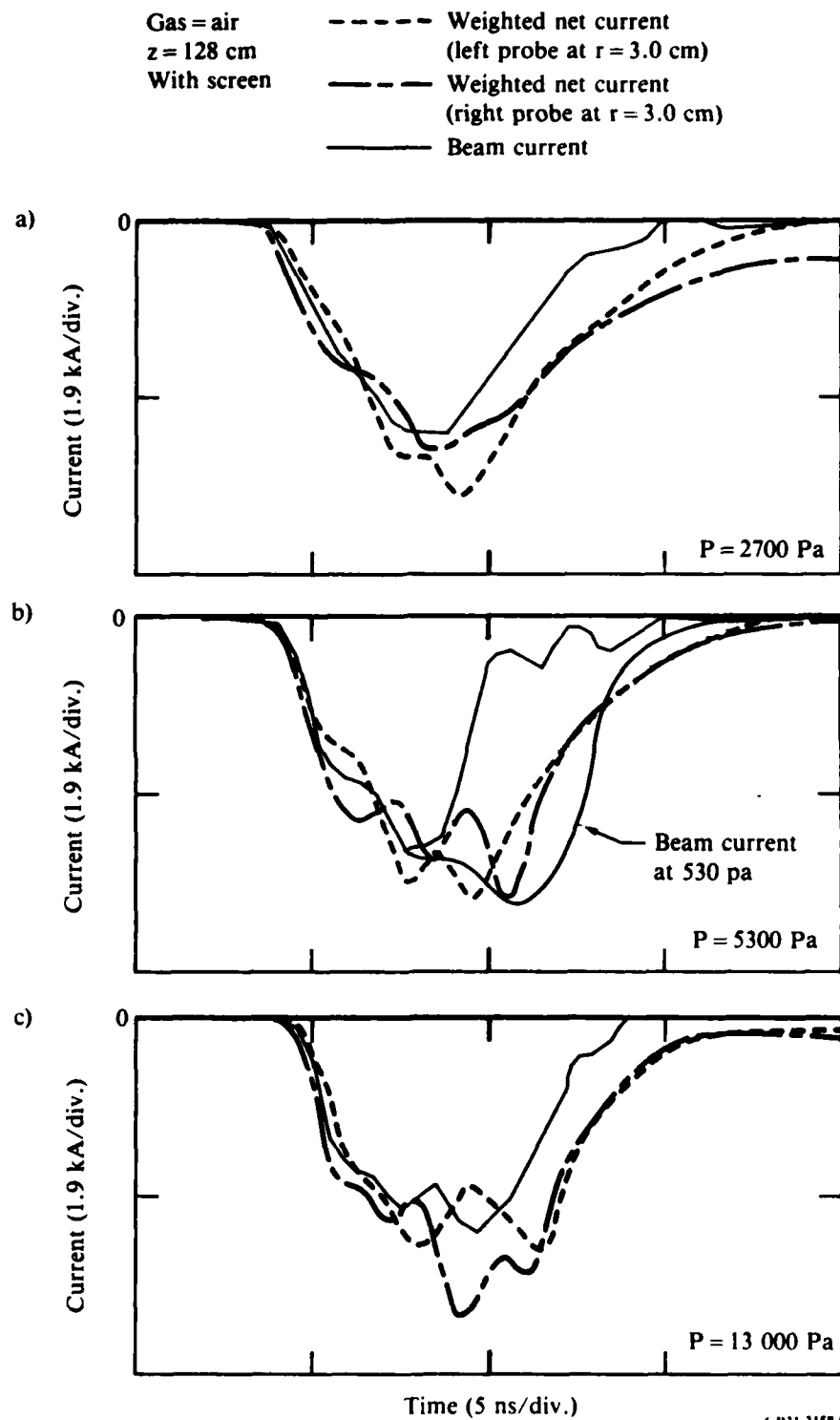


Figure 21. Net current as a function of time, weighted by a geometrical factor due to hose oscillations by the beam. Beam current is shown for comparison.

the monopole decay time, $\tau_m \approx \mu_0 \sigma a^2$, to be much larger than the beam pulse length. Decay times after the pulse are ~ 140 and 50 ns for the 130 and 400 Pa cases, respectively. At 1070 Pa, the return current decay time is reduced to ~ 15 ns, so that significant return current decay is observed within the pulse length. The values of σ implied by these decay times are much larger than expected from direct beam-produced ionization alone, implying substantial avalanche ionization.

For pressures of 2700 Pa and above (Figure 21) the probe signals are no longer symmetric between right and left sides, because of the motion of the beam. The interpretation of the probe signals can no longer be simply in terms of the net current based on cylindrical symmetry, i.e.,

$I_n = 2\pi r B_\theta / \mu_0$. Under the assumption, reasonable at these pressures, that the current flow diameter is small compared to the radius at which the observation is made, we can calculate that

$$B_y = \frac{\mu_0 I_n}{2\pi x_p} \times \frac{1 - \tilde{x}}{(1 - \tilde{x})^2 + \tilde{y}^2}, \quad (3)$$

where B_y is the magnetic field perpendicular to the plane of the loops of the magnetic-field probes, x_p is the position coordinate of the probe (y_p is zero), and \tilde{x} and \tilde{y} are the coordinates of the beam filament (normalized to x_p). This expression is derived by calculating the magnetic field of an off-center current filament at the probes, neglecting image currents. Based on Equation (3), the quantity $2\pi x_p B_y / \mu_0$ can be interpreted as I_n times the weighting factor $(1 - \tilde{x}) / (1 - \tilde{x})^2 + \tilde{y}^2$.

In Figure 21, we see that the Faraday cup data (taken on different shots but the same conditions) show the beam current and the net current to be equal in the early part of the pulse. In some cases, particularly those shown in Figures 21b and 21c, it appears that the beam is lost from the Faraday cup at earlier times than indicated from magnetic-probe measurements. This loss may be caused by a slight variation in beam behavior which produced greater loss of the beam tail for the Faraday cup shots. In Figure 21b, the Faraday cup data are replicated for 530 -Pa propagation, where the tail of the beam is stable. Apparently tail loss on the particular shot measuring these magnetic-probe data is between the losses seen in the two Faraday cup signals.

Some semi-quantitative conclusions can be inferred from these data. The first conclusion is that the near equality of beam current and net current indicates that avalanche ionization is small at 2700 Pa and above, for the low current case. The induced electric fields are sufficiently low (E_z peaks at ~ 2000 V/cm) that this deduction is quite reasonable. A second conclusion is that the hose frequency observed is roughly in accord with theory. The most unstable wave expected has a real frequency of $\omega \approx 1/\sqrt{3} \tau_d$, where τ_d is the dipole decay time (Reference 13). For a Bennett profile, $\tau_d \approx 1/8 \tau_m$, where τ_m is the monopole decay time (Reference 14). Thus, the period of the hose oscillations should be $\tau_{\text{hose}} = 2\pi/\omega = 2\pi\sqrt{3}/8 \tau_m \approx 1.4 \tau_m$. After the beam has passed, a decay time, τ_m , of ~ 2 ns was observed. During the beam pulse, τ_m should be less because τ_m is proportional to the plasma conductivity (which is proportional to the plasma electron density) which increases over the length of the beam pulse. Thus $\tau_{\text{hose}} \lesssim 3$ ns is calculated, which is in accord with the observations.

For the high-beam-current case ($I_b \approx 8$ kA), the net current signals shown in Figure 22 indicate that current neutralization at high pressures is much greater than that observed for the low-current case. Compare Figures 22d and 21a. This increased neutralization probably results from the greater dI/dt at the beam front, resulting in some avalanche ionization. The resultant increased conductivity produces a larger τ_m (approximately ~ 20 ns at 2700 Pa by the end of the beam pulse) and thus the return current does not decay as quickly (i.e., the net current is frozen at a low value by the avalanche-generated conductivity). A quantitative comparison of the measured net current with that predicted by a circuit model is planned and may be able to explain the difference between the high- and low-current data.

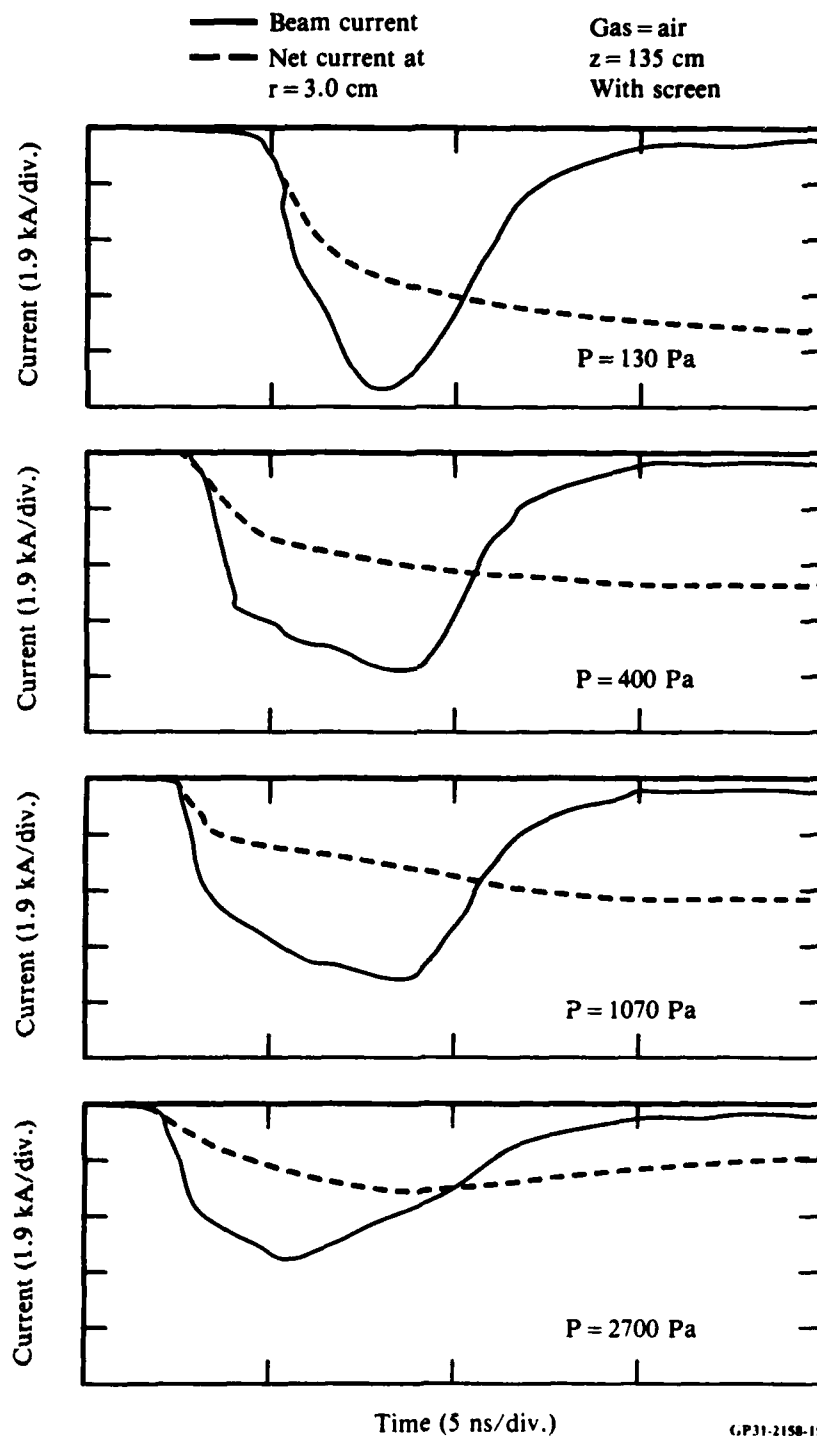


Figure 22. Net current data with screen inside the glass drift tube at a higher beam current ($I_{\text{beam}} \cong 8$ kA).

IV. SUMMARY AND CONCLUSIONS

Propagation experiments have been conducted with a 1-MeV, 10-ns electron beam with currents of 2-8 kA, in a 7.6-cm-diam glass tube, in the same tube with a conducting screen inside, and in a 3.4-m-diam chamber.

A pressure window for good propagation exists between 200 and 1070 Pa of air for propagation in a glass guide tube with no screen at a beam current of 6 kA. The net current is ~ 1 kA, implying a large plasma return current within the beam volume. The net current is observed to be in the beam direction over a broad radial profile of ~ 2.5 -cm radius, compared to a beam radius of ~ 0.5 cm; these are similar to observations on ETA at LLNL. At lower pressures, the entire beam deflects and strikes the tube; at higher pressures, the beam tail is lost, with increasing loss as the pressure is increased. At low current (2.4 kA) the loss of the tail at high pressure is more severe. With the screen inside the drift tube, ion-focused-regime propagation is observed. For pressure•time products, $Pt \cong 100$ Pa•ns, a notch in beam current propagated is observed, probably due to the two-stream instability. At pressures of 130-1070 Pa a propagation window is observed, similar to that without the screen, with a broad forward net current radial profile. At higher pressures, the $m = 1$ hose instability is observed, with the net current equal to the beam current and loss of the tail of the beam. The observed hose-oscillation frequency is in reasonable accord with theory.

Propagation in the 3.4-m-diam chamber is rectilinear (within ~ 10 mrad) over only a narrow pressure range around 540 Pa.

The beam front velocity increases with pressure to a broad peak at ~ 1000 Pa, decreasing at much higher pressures. At low pressures, the lower current beam had faster front velocities.

V. RECOMMENDATIONS

For future study, the following comparisons with theory suggest themselves:

- (1) An envelope code following beam propagation in the ion-focused regime (IFR) should be compared with the IFR front-arrival data.
- (2) The high-pressure front velocity, net current, and hose growth data should be compared with simulation runs for the same beam parameters.
- (3) Measurements of microwave emission and of plasma density could clarify the role of the two-stream instability in producing the notch in beam current described in Section III D.

REFERENCES

1. The advantages of using a bow probe were suggested by J. Clark, Lawrence Livermore National Laboratory, private communication.
2. McDonnell Douglas Corporation Independent Research and Development Report on Charged Particle Beams, 1984, McDonnell Douglas Report MDC Q0871-4, p. 012.03 (in press).
3. M. A. Greenspan, "Short-Pulse Electron-Beam Propagation Experiments in a Controlled-Environment Chamber," McDonnell Douglas Report MDC Q0762, 8 March 1982.
4. R. J. Briggs, "A Simple Model of Beam Transport in Low-Pressure Ion-Focused Regimes," Lawrence Livermore National Laboratory Report UCID-19187, 1981.
5. T. J. Fessenden, R. J. Briggs, J. C. Clark, E. J. Lauer, and D. O. Trimble, "FX-25 Beam Propagation Experiments," Lawrence Livermore National Laboratory Report UCID-17840, 1978.
6. P. A. Miller, J. B. Gerardo, and J. W. Poukey, "Relativistic Electron-Beam Propagation in Low-Pressure Gases," *J. Appl. Phys.* 43, 3001 (1972).
7. P. A. Miller and J. B. Gerardo, "Relativistic Electron Beam Propagation in High-Pressure Gases," *J. Appl. Phys.* 43, 3008 (1972).
8. F. W. Chambers and J. A. Masamitsu, "Beam Erosion Rates--Comparison of Analytic and Computed Results," Lawrence Livermore National Laboratory Report UCID-18746, 1980.
9. S. A. Bludman, K. M. Watson, and M. N. Rosenbluth, "Statistical Mechanics of Relativistic Streams," *Phys. Fluids* 3, 747 (1960).
10. E. P. Lee, F. W. Chambers, L. L. Lodestro, and S. S. Yu, "Stable Propagation of an Electron Beam in Gas," in Proceedings of 2nd International Topical Conference on High-Power Electron and Ion Beams (Cornell University, Ithaca, NY, 1977), p. 381.
11. G. Knop and W. Paul, "Interaction of Electrons and α -Particles with Matter," in Alpha-, Beta-, and Gamma-Ray Spectroscopy, ed. by K. Siegbahn, (North-Holland, Amsterdam, 1965), p. 16.
12. S. S. Yu and R. E. Melendez, "Model of Current Enhancement at High Pressure," Lawrence Livermore National Laboratory Report UCID-19965, 1983.

13. E. P. Lee, "Resistive Hose Instability of a Beam With the Bennett Profile," Phys. Fluids 21, 1327 (1978).
14. W. Barletta, "The Complete Back of the Beam Envelope Calculations," Lawrence Livermore National Laboratory Report UCID-19152, 1981.

DISTRIBUTION LIST

	<u>COPIES</u>
Department of the Navy Chief of Naval Operations Attn: Dr. Charles F. Sharn (UP-987B) Deputy Director of Research and Development Plans Division Washington, DC 20350	1
Defense Technical Information Center Cameron Station Alexandria, VA 22314	12
Director, Defense Advanced Research Projects Agency Attn: LTCOL R. L. Gullickson Dr. J. Manyano 1400 Wilson Boulevard Arlington, VA 22209	1 1
JAYCOR 205 S. Whiting Street Attn: Dr. R. Hubbard Alexandria, VA 22304	1
Department of Energy Attn: Dr. Marshall Sluyter Office of Inertial Fusion DP-231 Washington, DC 20545	1
Department of the Navy Chief of Naval Research Attn: Dr. T. Berlincourt/Dr. W. Condell, Code (410) 800 North Quincy Street Arlington, VA 22217	1
Commander Naval Sea Systems Command Department of the Navy Attn: CAPT Robert L. Topping (PMS-405) Mr. A. L. Stoessel (PMS-405) Washington, DC 20362	1

Commanding Officer
Naval Research Laboratory
Attn: Dr. J. Greig (Code 4763)
Dr. M. Lampe (Code 4792)
Dr. I. Vitkovitsky (Code 4770)
Dr. M. Friedman (Code 4700.1)
Dr. A. Robson (Code 4760)
Dr. M. Raleigh (Code 4763)
Washington, DC 20375

1
1
1
1
1
1
1

Superintendent
Naval Postgraduate School
Physics Department
Attn: Dr. K. E. Woehler
Monterey, CA 93940

1

U. S. Army Ballistic Research
Laboratory
Attn: Dr. D. Eccleshall (BRDAR-BLB)
Aberdeen Proving Ground, MD 21005

1

Commander
Harry Diamond Laboratories
Attn: Mr. S. Graybill (Branch 22900)
2800 Powder Mill Road
Adelphi, MD 20783

1

Director, Ballistic Missile Defense
Advanced Technology Center
Attn: Mr. Milton Hawie (BMSATC-1)
P. O. Box 1500
Huntsville, AL 35807

1

Air Force Office of Scientific Research
Attn: CAPT H. L. Pugh, Jr.
Physical and Geophysical Sciences
Bolling Air Force Base
Washington, DC 20332

1

Air Force Weapons Laboratory
Kirtland Air Force Base
Attn: Dr. David Straw, Code NTYP
Albuquerque, NM 87117

1

Department of Commerce
National Bureau of Standards
Attn: Dr. Penner, Bldg. 245, B-102/
Dr. Wilson, Bldg. 245, B-102
Washington, DC 20234

1

Lawrence Livermore National Laboratory
University of California

Attn: Dr. R. Briggs (L-321)
Dr. T. Fessenden (L-436)
Dr. W. Barletta (L-321)
Dr. D. Prono (L-436)

1
1
1
1

P. O. Box 808
Livermore, CA 94550

Los Alamos National Laboratory

Attn: Dr. Thomas P. Starke,
Mail Stop 5000

1

P. O. Box 1663
Los Alamos, NM 87545

Union Carbide Corporation

Nuclear Division

Oak Ridge National Laboratory

X-10 Laboratory Records Department

P. O. Box X

Attn: Dr. R. Ritchie

Oak Ridge, TN 37830

1

AVCO-Everett Research Laboratory, Inc.

Attn: Dr. R. Patrick/Dr. D. Reilly

2385 Revere Beach Parkway

Everett, MA 02149

1

Cornell University

Attn: Prof. David Hammer

Ithaca, NY 14853

1

Foreign Technology Division

Attn: Mr. C. J. Butler/TJTD

Wright Patterson AFB, OH 45433

1

The Charles Stark Draper Laboratory, Inc.

Attn: Mr. E. Olsson

555 Technology Square

Cambridge, MA 02139

1

Directed Technologies, Inc.

Attn: Mr. Ira F. Kulin, Jr.

1226 Potomac School Road

McLean, VA 22101

1

La Jolla Institute

Attn: Dr. K. Brueckner

P. O. Box 1434

La Jolla, Ca 92038

1

Lockheed Missile & Space Co., Inc.
Attn: Dr. J. Siambis
3251 Hanover Street
Building 203, Dept. 52-11
Palo Alto, CA 94304

1

Mission Research Corporation
Attn: Dr. Brendan B. Godfrey,
Plasma Sciences Division
EM System Applications Division
1720 Randolph Road, SE
Albuquerque, NM 87106

1

Mission Research Corporation
Attn: Dr. N. Carron
P. O. Drawer 719
Santa Barbara, CA 93102

1

Pulse Sciences, Inc.
Attn: Dr. S. Putnam
14796 Wick Boulevard
San Leandro, CA 94577

1

Sandia National Laboratories
Attn: Mail Stop Section for
Dr. R. B. Miller
P. O. Box 5800
High Energy Beam Physics Division - 1246
Albuquerque, NM 87185

1

Science Applications, Inc.
Attn: Dr. R. Johnston
5 Palo Alto Square, Suite 206
Palo Alto, CA 94306

1

SRI International
Attn: Dr. Donald J. Eckstrom
333 Ravenswood Avenue
Menlo Park, CA 94025

1

Titan Systems, Inc.
Attn: Dr. R. M. Dowe
9191 Towne Centre Drive
Suite 500
San Diego, CA 92122

1

TRW Electronics and Defense Sector
Attn: Dr. D. Arnush/Dr. John Bayless, R1/1078
One Space Park
Redondo Beach, Ca 90278

1

Naval Surface Weapons Center

Attn: Dr. C. M. Huddleston (R401)

Dr. E. E. Nolting (F53)

Dr. H. S. Uhm (R41)

Dr. M. F. Rose (F04)/Mr. K. C. Baile (F10)

Mr. R. L. Vergy (F10)

Mr. R. J. Biegalski (N13)

Dr. R. Cawley (R41)

Dr. J. Forbes (R13)

Dr. R. B. Fiorito (R41)

Library (E43 - CHAIR HERITAGE Data Bank)

Silver Spring, MD 20910

1
1
1
1
1
1
1
1
1
1